THE ASTROPHYSICAL JOURNAL, 487:346–364, 1997 September 20
© 1997. The American Astronomical Society. All rights reserved. Printed in U.S.A.

THE STAR-FORMING CORE OF MONOCEROS R2

JEAN GIANNAKOPOULOU,[1] GEORGE F. MITCHELL,[2] AND TATSUHIKO I. HASEGAWA
Department of Astronomy and Physics, Saint Mary's University, Halifax, NS, Canada B3H 3C3
HENRY E. MATTHEWS
Joint Astronomy Centre, University Park, 660 North A'ohoku Place, Hilo, HI 96720-6030
AND
JEAN-PIERRE MAILLARD[2]
Institute d'Astrophysique, 98 bis, Boulevard Arago, F-75014, Paris, France
Received 1996 May 15; accepted 1997 April 22

ABSTRACT

The central region of the Monoceros R2 molecular cloud has been studied using molecular line maps, maps in continuum emission, and an M-band (4.7 μm) absorption spectrum toward Mon R2 IRS 3. Maps were made in the emission lines CO (3–2) H_2CO ($5_{1,5}$–$4_{1,4}$), and HCN (4–3), all with a 14″ beam size. CO (2–1) and ^{13}CO (3–2) spectra were obtained at a dozen positions. Maps of continuum emission were made at 1300 μm (25″ resolution), 1100 μm (20″ resolution), 800 μm (14″ resolution), and 450 μm (14″ resolution). The M-band spectrum of IRS 3 has a velocity resolution of 5.2 km s^{-1} and shows fundamental vibrational band absorption lines of CO and ^{13}CO over a range of rotational states. The CO map has numerous intensity peaks which, if interpreted as clumps, have masses from 0.1 to 3 $M_\odot$. The large velocity dispersion of these structures implies that they cannot be gravitationally bound. The brightest CO-emitting gas shows no bipolar distribution with velocity. Diffuse CO-emitting gas with low velocities does have a generally bipolar distribution, but there are no collimated lobes pointing to a particular source. We conclude that the source (or sources) of the very extended Mon R2 outflow is (are) now inactive. The highest velocity gas is found toward the embedded young stellar object IRS 3, suggesting that IRS 3 is the source of a compact outflow, unresolved at our 14″ resolution. The presence of blueshifted CO in the absorption spectrum supports the interpretation of IRS 3 as an outflow source. The H_2CO and HCN maps demonstrate that much of the dense gas is distributed within three structures having different velocities. The fundamental band absorption lines of ^{13}CO show two gas temperatures in the line of sight to IRS 3. The colder (45 K) is identified as gas in the clump surrounding IRS 3, which is seen in emission lines of CO, H_2CO, and HCN. The warmer (310 K) we interpret as gas very close to IRS 3. From the submillimeter continuum maps we identify 11 clumps whose masses lie in the range 3–10 $M_\odot$. A clump that is prominent in the continuum maps but not in the molecular line maps is attributed to heated dust inside the compact H II region, where molecules have been destroyed.

Subject headings: ISM: individual (Monoceros R2) — ISM: jets and outflows — ISM: molecules

1. INTRODUCTION

Monoceros R2 is an association of B1–B9 stars illuminating nine reflection nebulae (van den Bergh 1966). The stars and reflection nebulosity lie in a giant molecular cloud, also referred to as Mon R2. Since its discovery by CO $J = 1$–0 mapping (Loren, Peters, & Vanden Bout 1974), the molecular cloud has been studied using centimeter and millimeter line emissions from of a variety of species including CS (Kutner & Tucker 1975; Linke & Goldsmith 1980; Montalbán et al. 1990; Wolf, Lada, & Bally 1990; Heyer et al. 1986; Tafalla, Bachiller, & Wright 1994), HCN (Kutner & Tucker 1975; Richardson et al. 1988), H_2CO (Loren et al. 1974; Downes et al. 1975), NH_3 (MacDonald et al. 1981; Willson & Folch-Pi 1981; Torrelles et al. 1983; Montalbán et al. 1990; Torrelles et al. 1990), and HCO^+ (Loren 1977; Richardson et al. 1988; Gonatas, Palmer, & Novak 1992).

The central region of the Mon R2 cloud is a site of ongoing star formation, as shown by the presence of a well-developed molecular outflow (Bally & Lada 1983; Wolf et al. 1990; Meyers-Rice & Lada 1991), a compact H II region (Massi, Felli, & Simon 1985; Wood & Churchwell 1989), an infrared cluster (Beckwith et al. 1976; Thronson et al. 1980; Hodapp 1987; Aspin & Walter 1990; Howard, Pipher, & Forrest 1994), and H_2O and OH masers (Downes et al. 1975; Knapp & Brown 1976). Most molecular maps with sufficient angular resolution show a similar appearance for the inner several-arcminute diameter core: the intensity of line emission has two peaks, in the northeast and the southwest, and surrounds an almost circular region of minimum intensity. The circular minimum coincides in position with, and is similar in size to, the compact H II region (diameter 22″). Images at 2.2 μm (Hodapp 1987; Aspin & Walter 1990; Howard et al. 1994) show a ring of emission surrounding IRS 1 and IRS 2. This emission can be understood as reflection from a dust shell surrounding the H II region.

The Mon R2 outflow is one of the largest known, with a total extent of 6.8 pc (assuming a distance of 950 pc; Racine & van den Bergh 1970). The center of the outflow is located at the infrared cluster, but its source has not yet been identified. The observations reported in this paper began as an attempt to identify the source of the CO outflow. We obtained a high-resolution (14″) CO $J = 3$–2 map that showed complex spatial and velocity structure, motivating us to map in the high-density tracers HCN and H_2CO and

[1] Present address: Department of Physics, University of Waterloo, Waterloo, ON, Canada N2L 3GL.
[2] Visiting Astronomer, Canada-France-Hawaii Telescope, operated by the NRC of Canada, the CNRS of France, and the University of Hawaii.

in the millimeter-submillimeter continuum, all at similar angular resolutions. A 4.6 μm spectrum of IRS 3 at high spectral resolution was obtained, providing an independent measure of gas properties in the cloud core. All these data have been combined into the present study of the inner $3' \times 3'$ core of the Mon R2 cloud.

Details of the observations are given in § 3. In § 4, gas properties are found from spectra in the three transitions CO $J = 3$–2, CO $J = 2$–1, and ^{13}CO $J = 2$–1. Section 5 contains an analysis of the infrared CO absorption lines. The distribution and kinematics of dense gas, as seen in HCN and H_2CO maps, are discussed in § 6. Maps of continuum emission at 450, 800, 1100, and 1300 μm are presented in § 7. Conclusions are summarized in § 8.

2. OBSERVATIONS

All emission line spectra were obtained with the 15 m James Clerk Maxwell Telescope (JCMT) on Mauna Kea over several observing periods in 1991 and 1992. Line observations were carried out using position switching, in which the telescope was alternated between the source and a nearby reference position with no emission. Only linear baselines were removed from spectra. A CO $J = 3$–2 map was obtained, consisting of 290 spectra covering most of an area 150″ in right ascension by 180″ in declination on a 10″ grid. At 345 GHz, the half-power beamwidth (HPBW) was 14″ (0.06 pc at the distance of Mon R2) and the beam efficiency was 0.50 (Matthews 1992). CO $J = 2$–1 and ^{13}CO $J = 3$–2 spectra were obtained at 12 positions, namely, (0, 0), (10, 20), (−10, −20), (−10, 60), (−20, −70), (−20, −10), (−20, 40), (−40, −40), (−40, 60), (−50, −60), (−60, −10), (−80, 30). Here and subsequently, positions are given as offsets in right ascension and declination in arcseconds $(\Delta\alpha, \Delta\delta)$ from Mon R2 IRS 3 [$\alpha(1950) = 06^h05^m21^s.50$, $\delta(1950) = -06°22'26''$]. East and north are positive. At the 230 GHz frequency of the CO $J = 2$–1 transition, the HPBW and beam efficiency were 21″ and 0.63, respectively (Matthews 1992). Maps in HCN $J = 4$–3 (354.5 GHz) and H_2CO $J_{K-1,K+1} = 5_{1,5}$–$4_{1,4}$ (351.7 GHz) were obtained over an area 180″ in right ascension by 160″ in Declination.

Continuum maps of the inner 3′ of the Mon R2 region were obtained with the facility single-element bolometer receiver (Duncan et al. 1990). The data in this paper were obtained with the filters at 450, 800, 1100, and 1300 μm, for which the beamwidth to half-power is in the range 16″–27″ at full aperture. For the shorter wavelengths, 450 and 800 μm, we narrowed the aperture to obtain diffraction-limited maps. The final effective angular-resolution was set in the data analysis stage, for which we used the NOD2 package (Haslam 1974). The reduced maps have angular resolution of 14″, 14″, 20″, and 25″, respectively. The maps were obtained in the standard way, i.e., by scanning along lines of constant azimuth through the source field while using the chopping subreflector to obtain the difference at a chop rate of 7.8 Hz between two beam positions (right and left beams) separated in azimuth. The chop throw was selected to be typically 2 or 3 times the half-power beamwidth; either 30″, 40″, or 60″. The spacing between grid points both in the scan direction and orthogonal to it was either 2″, 4″, or 6″, chosen to be typically one-third to one-quarter the beam size. A complete map consisted of a series of scans through both right and left beams in azimuth, stepped by the grid spacing in elevation. A typical map consisted of 55 points in azimuth by 45 points in elevation, and since the integration time per point was 1 s, such a map lasted typically 40 minutes. Photometric calibration was carried out at each of the filter/aperture combinations by observing Mars and CRL 618 at a range of air masses throughout the observing period. From these data the response of the bolometer system and the zenith opacity for each instrumental setup was obtained. The flux densities of Mars at the various filter wavelengths were obtained from a program that uses the model developed by Wright (1976), and those for CRL 618 were taken from Sandell (1994). The total error in the flux density scale should be no more than 15% at 1300 μm and 30% at 450 μm.

On 1991 January 3, Mitchell and Maillard used the Fourier transform spectrometer (FTS) of the Canada-France-Hawaii Telescope on Mauna Kea to obtain a high-resolution infrared M-band (4.7 μm) spectrum of source IRS 3 in the infrared cluster. We employed a filter with a passband from 2080 to 2180 cm^{-1} (4.59–4.81 μm), encompassing the central region of the fundamental band of both CO and ^{13}CO. Beam switching of the source between the two entrance apertures was used to cancel the thermal background. The thermal background was further reduced by the use of a small aperture of 2″.5. A spectral resolution of 0.037 cm^{-1} was used, corresponding at 4.7 μm to $\lambda/\Delta\lambda = 57{,}000$ with a velocity resolution of 5.2 km s^{-1}. The total observing time on IRS 3 was 50 minutes, and the final spectrum has a signal-to-noise ratio (1 σ) of 26. Correction for absorption lines in the Earth's atmosphere was accomplished by dividing the IRS 3 spectrum by a spectrum of the Moon taken on the same night.

3. MORPHOLOGY AND KINEMATICS OF THE CO-EMITTING GAS

Figure 1 shows CO $J = 3$–2 and ^{13}CO $J = 3$–2 spectra for six positions in the map. In Figure 1 and in the integrated intensity maps that follow, we use T_r^* as a measure of the observed temperature, where $T_r^* = T_A^*/\eta_{\rm fss}$. T_A^* is the antenna temperature corrected for telescope and atmospheric losses. For the JCMT at 345 GHz, $\eta_{\rm fss} = 0.70$. It is clear that the CO lines are extraordinarily complex and vary a great deal with position. The ^{13}CO lines (as well as lines of high gas density tracers such as CS and H_2CO) peak at a velocity near $v_{\rm LSR} = 10.3$ km s^{-1}. Hereafter, we use the term *blueshifted gas* for gas with velocity less than 10.3 km s^{-1} and the term *redshifted gas* for gas with velocity greater than 10.3 km s^{-1}. Over the mapped region, two absorption features are present in most of the spectra, one near 7.6 km s^{-1} and the other near 11.3 km s^{-1}. The minimum at 7.6 km s^{-1} is probably due to a foreground cloud. The feature at 11.3 km s^{-1}. The minimum at 7.6 km s^{-1} is probably due to a foreground cloud. The feature at 11.3 km s^{-1} is redshifted by only 1 km s^{-1} relative to the bulk of the gas and may also be caused by a foreground cloud, but it could be formed in a contracting envelope surrounding the core. A dip near 16.4 km s^{-1}, which is seen in many spectra across the mapped region, is not due to absorption but appears to be a true emission minimum.

Figure 2 shows the intensity of CO $J = 3$–2 emission integrated over all velocities. There are three main regions of strong CO emission, one in the north, one in the east, and one in the southwest. They are distributed around an almost circular area of low intensity. The CO emission almost encloses the central low-intensity region, except for a gap to the northwest. In Figure 3, maps of integrated inten-

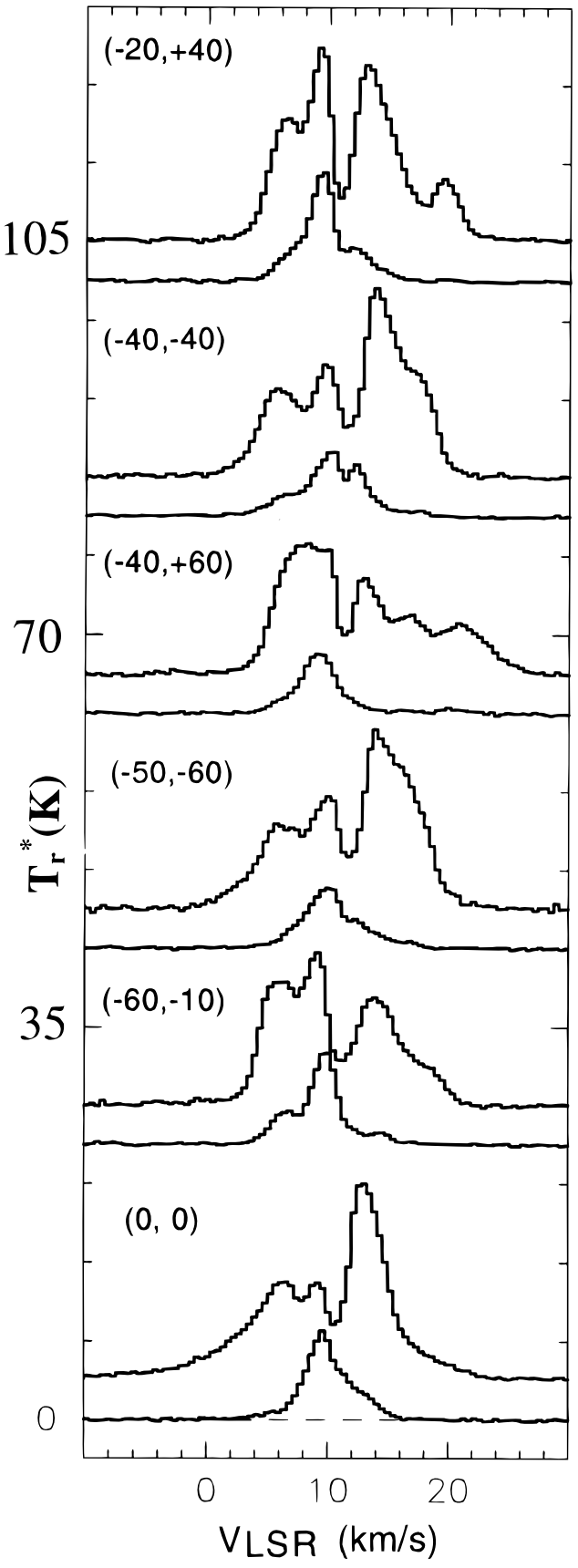

FIG. 1.—CO $J = 3$–2 and ^{13}CO $J = 3$–2 spectra at six positions. At each position, the upper spectral line is CO and the lower is ^{13}CO. Positions are given as offsets in arcseconds from IRS 3 at $\alpha(1950) = 06^h05^m21^s.50$, $\delta(1950) = -06°22'26''$.

sity are shown in 1 km s^{-1} channels over the range $0 \leq v_{LSR} \leq 29$ km s^{-1}. The channel maps in the velocity interval 9–12 km s^{-1} are not shown because of the absorption features in this velocity range. At the highest blueshifted velocities in Figure 3*a*, there is significant emission only at the position of IRS 3. At lower velocities, other features appear. Figures 3*b* and 3*c* shows the general morphology of the redshifted gas.

An examination of the redshifted and blueshifted gas in Figure 3 does not show obvious evidence for bipolarity. In fact, the brighter blueshifted and redshifted emission peaks are distributed more or less randomly about the center. The highest velocity blueshifted gas is associated with IRS 3, but there is no evidence of a bipolar distribution of gas about IRS 3. On the other hand, there is a tendency for widespread, diffuse blueshifted gas to be concentrated toward the northern part of the mapped region, while a redshifted diffuse component lies preferentially to the south. This can be seen by comparing channel maps near 6 km s^{-1} with channel maps near 16 km s^{-1} (Fig. 3). The observed trend is consistent with the large outflow. The absence of small-scale flow features originating from any of the infrared sources probably indicates that the source of the large outflow is no longer active.

The channel maps (Fig. 3) show structure on a variety of scales. There are a number of intensity peaks with diameters from $\sim 15''$ to $\sim 30''$, each of which can be followed over some range of velocity. The individual CO emission peaks tend to group into larger structures or complexes. We have identified a total of 13 smaller emission peaks with seven complexes. Three of the complexes are largely redshifted, while four consist of largely blueshifted gas. Some of the structures appear at the same position in blueshifted and redshifted velocities but cannot be identified at velocities near the two absorption features at 11 and 8 km s^{-1}. The most natural explanation in such cases is that we are seeing a single structure with a broad velocity dispersion. When a blueshifted and a redshifted peak are seen at the same position, we will assume a single entity, even if it cannot be seen within 1 km s^{-1} of the two absorption features. The position and observed velocity range of each identified peak are given in Table 1.

Position-velocity diagrams provide another tool for identifying velocity structure in data cubes. We show two such diagrams in Figure 4, each being a cut through the map in declination at constant right ascension. The narrow feature through the center of the two position-velocity diagrams is due to the 11 km s^{-1} absorption feature in the CO emission lines. Several of the intensity peaks listed in Table 1 can be seen in Figure 4, namely, peaks 1 and 6 (*top panel*) and peaks 3, 7, and 12 (*bottom panel*). Peak 6 at $(-5'', 55'')$ appears double, being cut in two by the absorption at 11 km s^{-1}. It seems reasonable to assume that we are seeing a single physical structure with a very broad range of velocity ($\sim$3–29 km s^{-1} in this case). Peak 12 at $(-55'', 50'')$, which we identified from velocity channel maps as purely redshifted, appears as an almost detached feature at 20 km s^{-1}.

The nature of the CO intensity peaks deserves further discussion. Are they in fact true clumps, or might they be temperature peaks caused, perhaps, by some internal heating process such as radiation from embedded young stellar objects? We do not have sufficient data to determine the CO excitation temperature at all positions in the mapped region. The temperatures at the CO emission

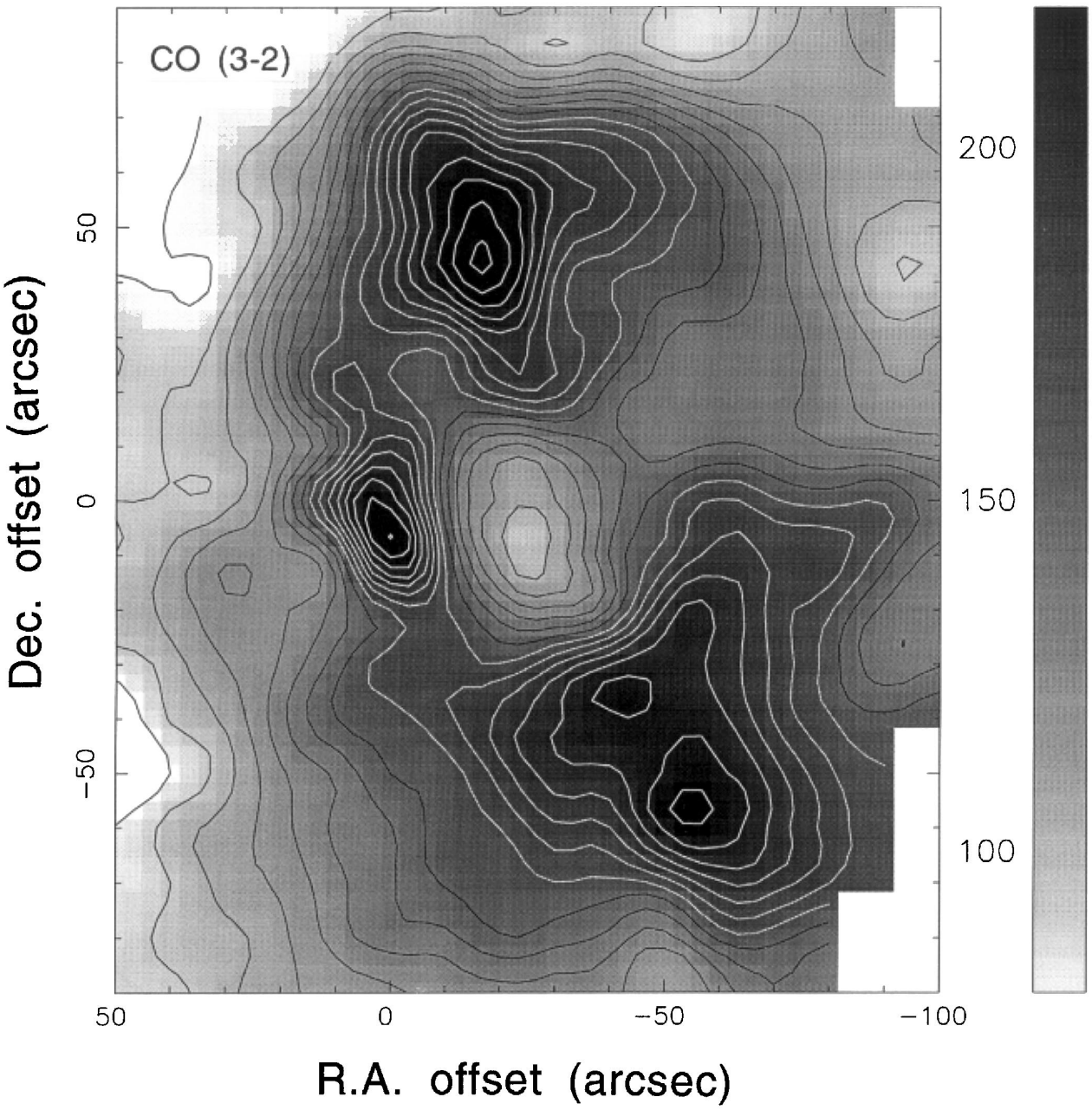

FIG. 2.—Intensity of CO $J = 3$–2 emission integrated over all velocities. Much of the intensity is organized into three main peaks which surround a relative minimum or "hole." The highest contour is 330 K km s^{-1}, and the contour interval is 14.3 K km s^{-1}. The map origin, (0, 0), is at IRS 3.

peaks, found as outlined in § 4.2 below, are near 40 K at low velocities (i.e., near the line center of 10 km s^{-1}) and show only moderate differences among the 12 positions. The emission peaks may be hot spots, or they may be true clumps (i.e., density peaks). A map of the entire region in a good temperature indicator, such as formaldehyde (Mangum & Wooten 1993), would certainly be desirable.

4. GAS PROPERTIES FROM THE CO EMISSION LINES

4.1. *Optical Depth*

The optical depth can be calculated from the ratio of radiation temperatures for two isotopes of CO. If we assume the solution of the transfer equation for a uniform medium in LTE, the antenna temperature, T_A^*, is related to the optical depth, τ_ν, of a rotational transition of frequency ν via the radiation temperature, T_R:

$$\frac{T_A^*}{\eta_B f} = T_R = (1 - e^{-\tau_\nu}) \frac{h\nu/k}{e^{h\nu/kT_{ex}} - 1}, \quad (1)$$

where η_B is the beam efficiency, f is the beam filling factor, and T_{ex} is the CO excitation temperature. Given antenna temperatures, T_A^{*12} and T_A^{*13}, for the two isotopomers ^{12}CO and ^{13}CO, the optical depth in a rotational transition can be evaluated from the ratio

$$\frac{T_R^{12}}{T_R^{13}} = \frac{T_A^{*12}}{T_A^{*13}} = \frac{1 - \exp(-\tau_\nu^{12})}{1 - \exp(-\tau_\nu^{13})} \quad (2)$$

To form the second quality of equation (2), we must make the assumption that both isotopomers have the same filling factor and excitation temperature. Finally, we assume an

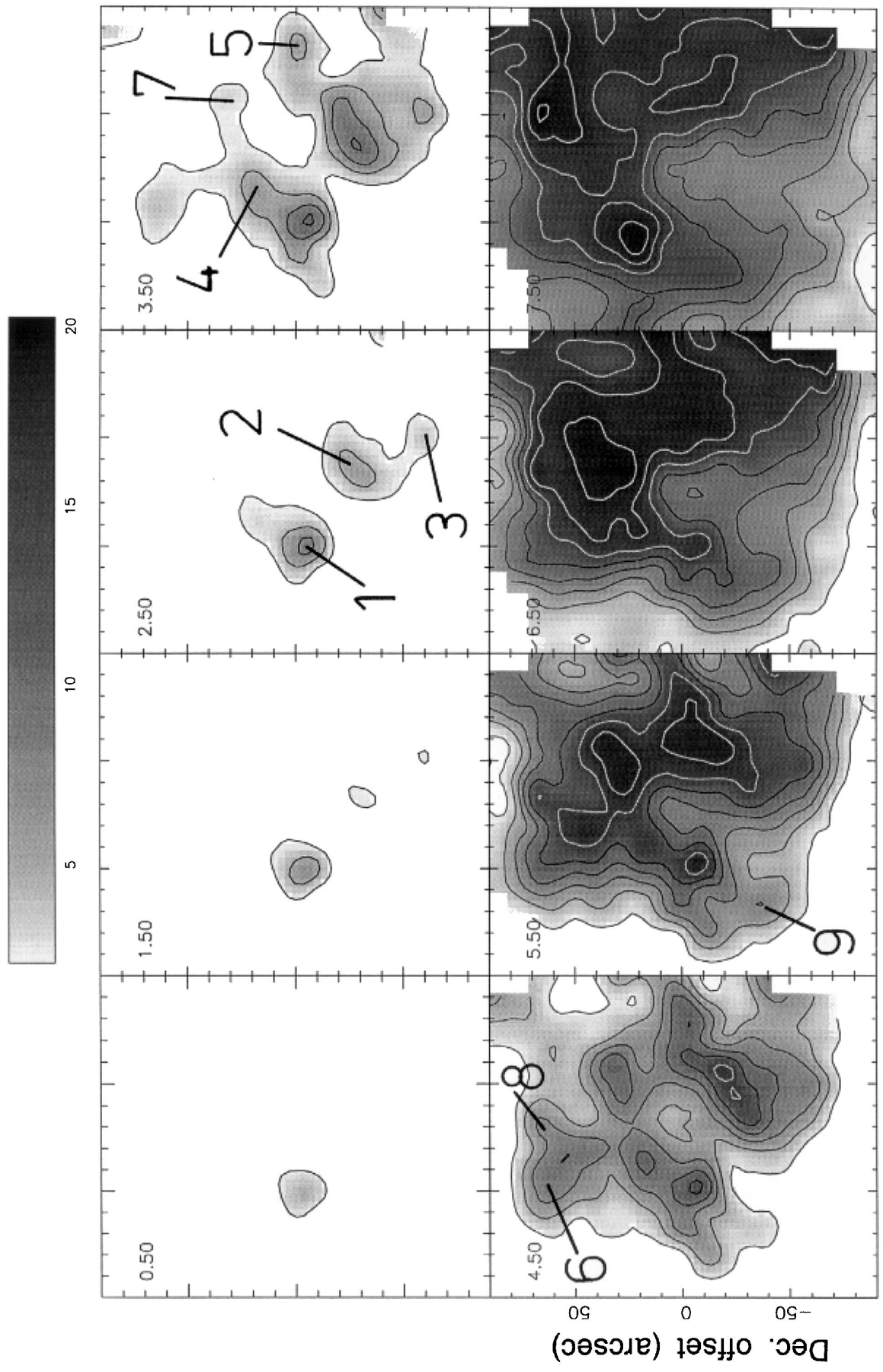

FIG. 3.—Integrated CO $J = 3$–2 intensity in 1 km s^{-1} channels from 0 to 29 km s^{-1}. The velocity interval 9–12 km s^{-1} is not shown because of the presence of absorption features in this velocity range. CO intensity peaks are labeled 1–13.

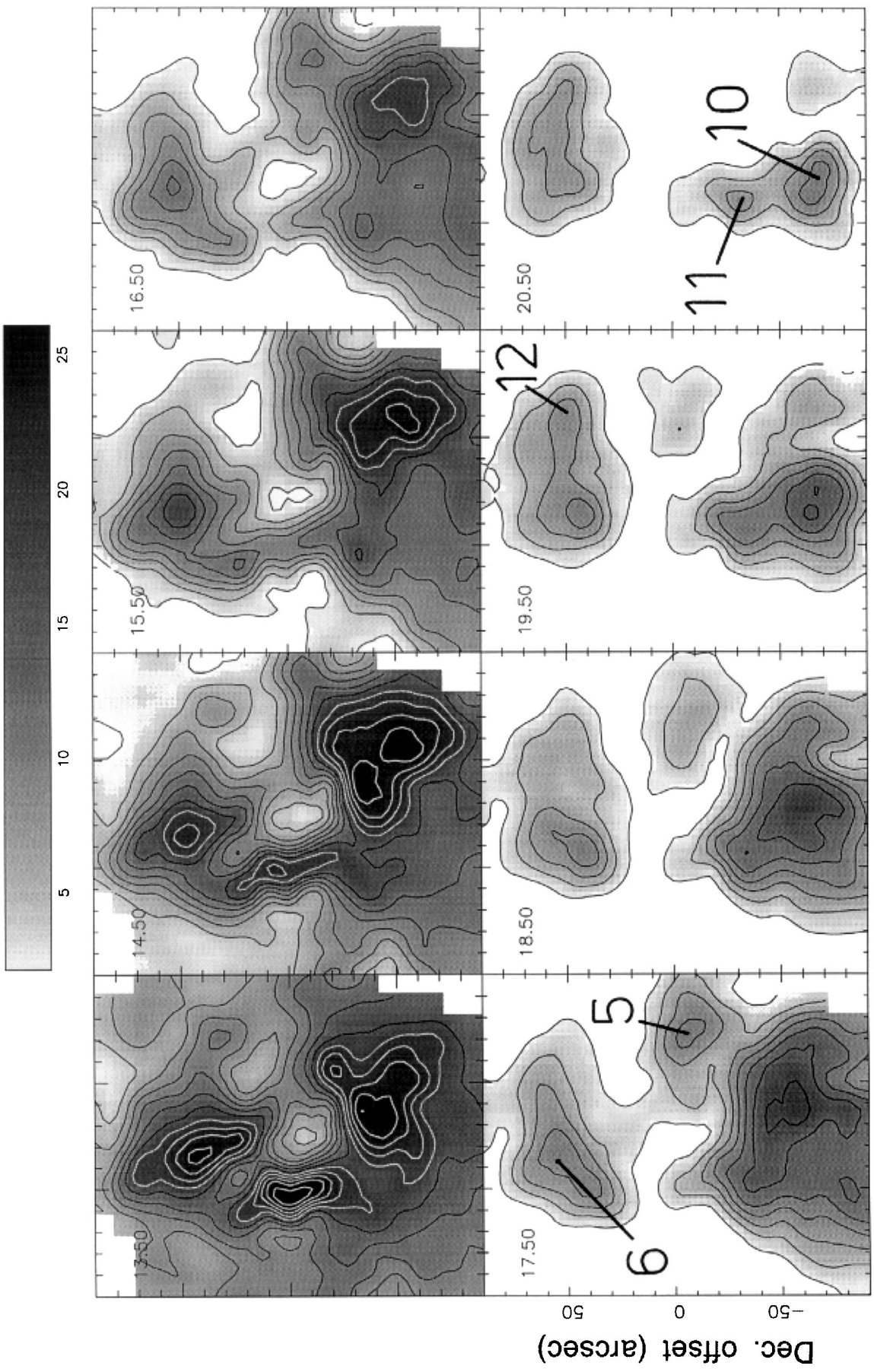

FIG. 3—*Continued*

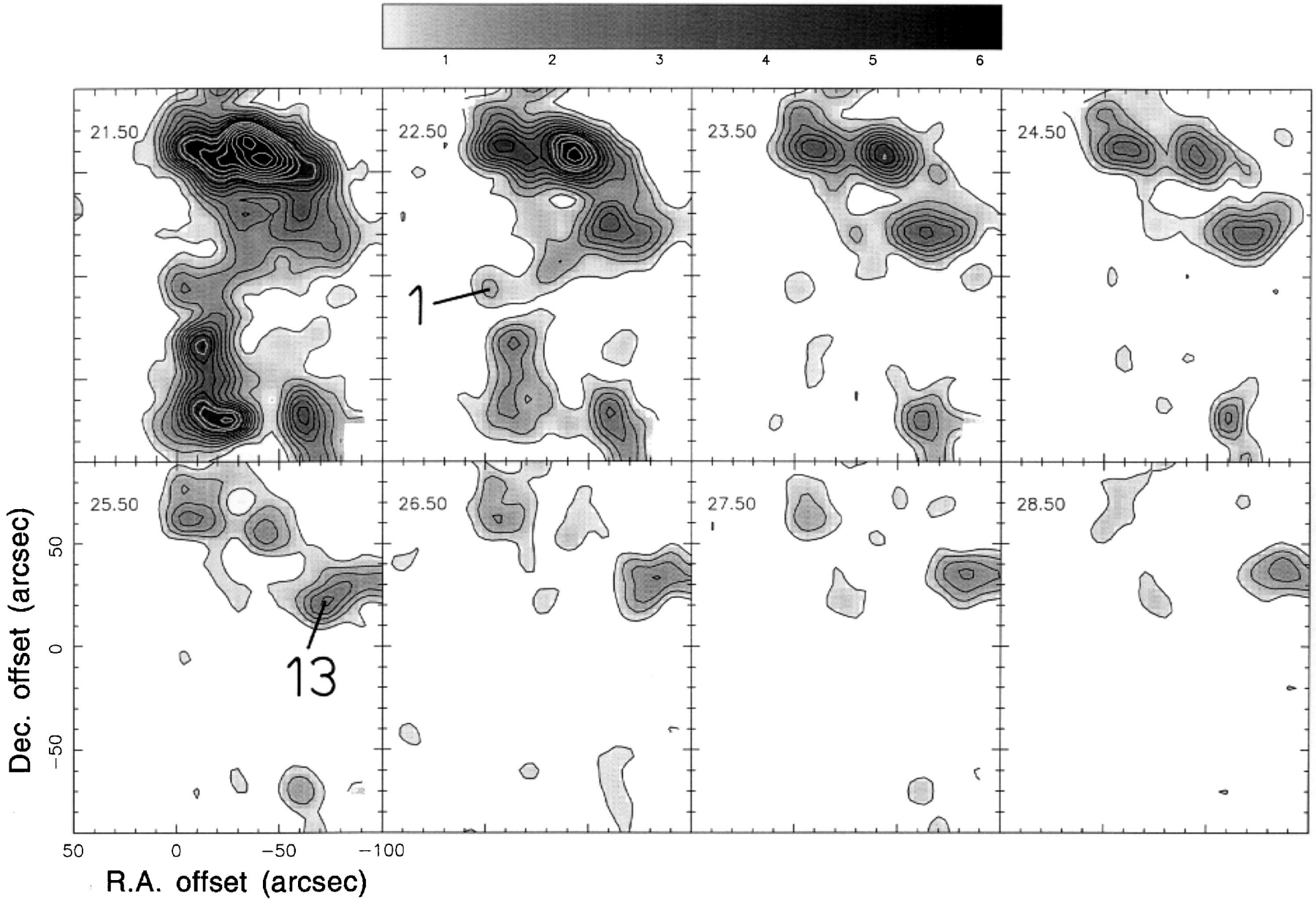

FIG. 3—*Continued*

TABLE 1

VELOCITY RANGE OF CO $J = 3$–2 EMISSION PEAKS

Identifying Number	Offsets from IRS 3	Velocity Range (km s^{-1})
1	0, −10	−40 to 35
2	−50, −20	−20 to 16
3	−50, −50	1 to 29
4	−50, 20	−15 to 9
5	−80, 0	3 to 20
6	−5, 55	3 to 29
7	−55, 30	−25 to 6
8	−30, 65	−5 to 9
9	15, −35	4 to 7
10	−20, −65	16 to 23
11	−10, −35	15 to 24
12	−55, 50	18 to 27
13	−75, 25	22 to 30

abundance ratio $^{12}CO/^{13}CO = 60$ (Langer & Penzias 1990), so that $\tau_v^{12} = 60\tau_v^{13}$, and equation (2) can be solved for τ_v^{13}. It should be noted that filling factors for ^{12}CO and ^{13}CO need not be equal. If the filling factor for ^{12}CO is larger than that for ^{13}CO, then from equation (2) our calculated optical depths will be systematically low. Optical depths were evaluated for the 12 positions where ^{13}CO spectra were available. The resulting optical depths as a function of velocity are presented in Figure 5 for the position of IRS 3. A common trend at all positions is that the optical depth peaks at a velocity close to the velocity of the cloud (10.3 km s^{-1}) and tends to decrease away from the line center. The maximum values of τ^{13} range between 1 and 3, while minimum values lie between 0.008 and 0.18. The minimum value is set by the detection limit of the ^{13}CO emission. For most positions there is a smooth variation of optical depth with velocity. Following Bevington (1969), we estimate the error in the value of the optical depth arising from uncertainties (noise) in the antenna temperature. The error in the optical depth varies from 8% near the line center to more than 20% for high-velocity gas. For some positions the antenna temperature of ^{13}CO near line center exceeds that of ^{12}CO, so that optical depths cannot be determined. A likely explanation for the inverted values is that ^{12}CO is optically thick and has a self-absorption dip, while ^{13}CO, being more optically thin, suffers less self-absorption.

In the calculations that follow, it is assumed that for velocities where ^{13}CO emission could not be detected, the gas is optically thin in the ^{12}CO line. The portion of the spectral line that has observable ^{13}CO emission is subsequently referred to as the *optically thick region*, whereas the rest of the line is referred to as the *optically thin region*. The use of the optically thin approximation where ^{13}CO is undetected appears to be satisfactory because the two regions yield compatible values for the excitation temperature and column density in the overlap region, as we shall see in the next sections.

4.2. *Excitation Temperature*

Once optical depths are known for the optically thick region of the spectrum, the excitation temperature ($T_{\rm thick}$) can be determined from equation (1) if the value of the filling factor is known. We adopt filling factors of unity. For velocities where ^{13}CO is undetected, the excitation temperature, $T_{\rm thin}$, is found from the two transitions CO

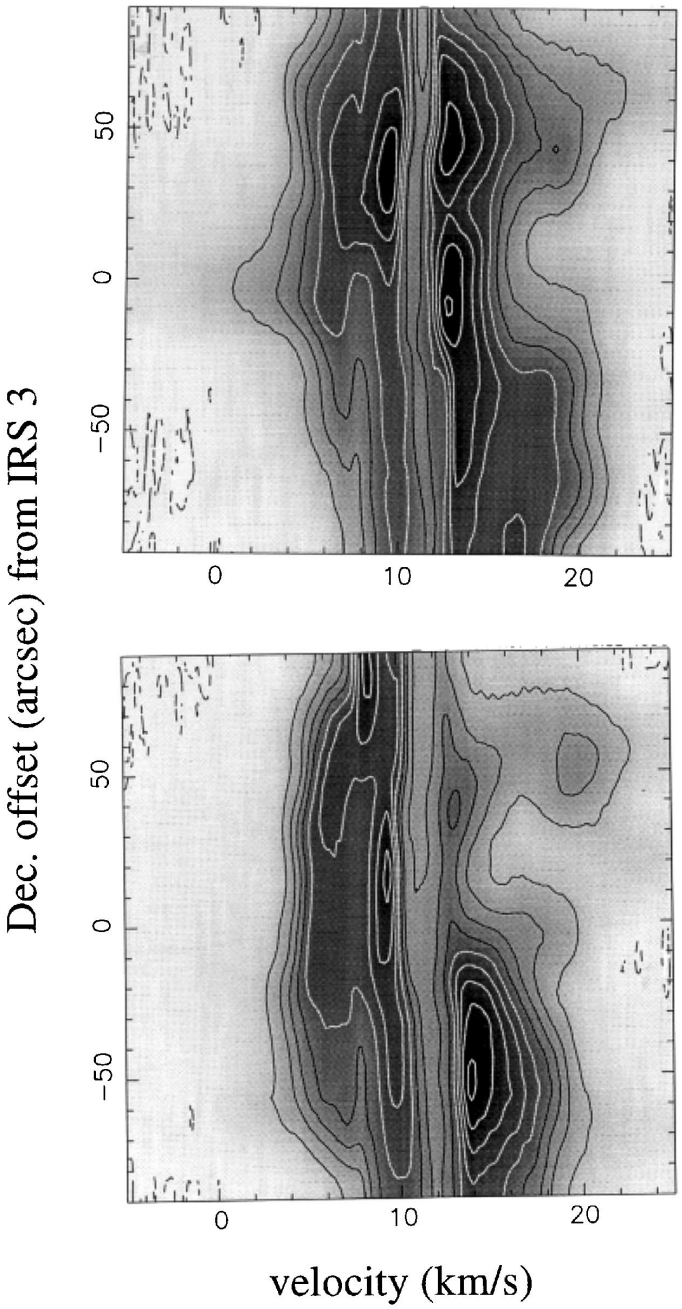

FIG. 4.—Position-velocity diagrams made from the CO (3–2) emission map shown in Fig. 2. Both panels represent a cut through the map in declination at a fixed right ascension. The narrow vertical band near 11 km s^{-1} is due to the absorption feature in the CO lines. The top panel is a cut at R.A. = −5″, showing peaks 1 and 6 of Table 1. The bottom panel is a cut at R.A. = −55″ and shows peaks 3, 7, and 12 of Table 1.

$J = 3$–2 and CO $J = 2$–1 by assuming the optically thin expression

$$T_{\rm thin} = -16.59\left[\ln\left(\frac{4}{9}\frac{T_R^{3\to2}}{T_R^{2\to1}}\right)\right]^{-1}, \qquad (3)$$

where it has been assumed that the filling factors of the two transitions are equal (but not necessarily unity). A plot of the excitation temperature versus velocity for the position of IRS 3 is presented in Figure 6. The decrease in temperature with increasing velocity from line center, seen in Figure 6, occurs at all 12 positions for which we are able to carry out this calculation. It is also the case at all positions

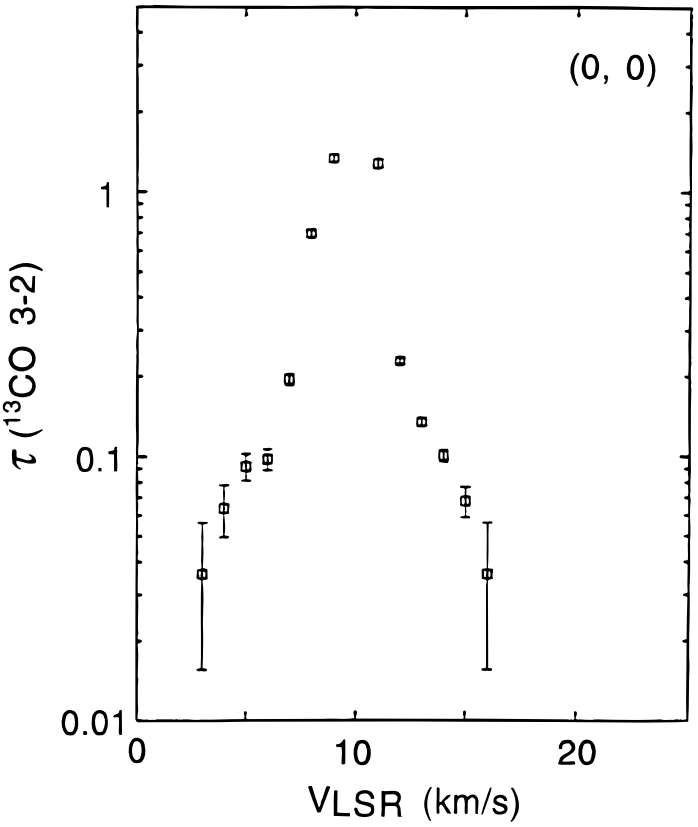

FIG. 5.—Optical depth in the ^{13}CO $J = 3$–2 line as a function of v_{LSR} towards IRS 3.

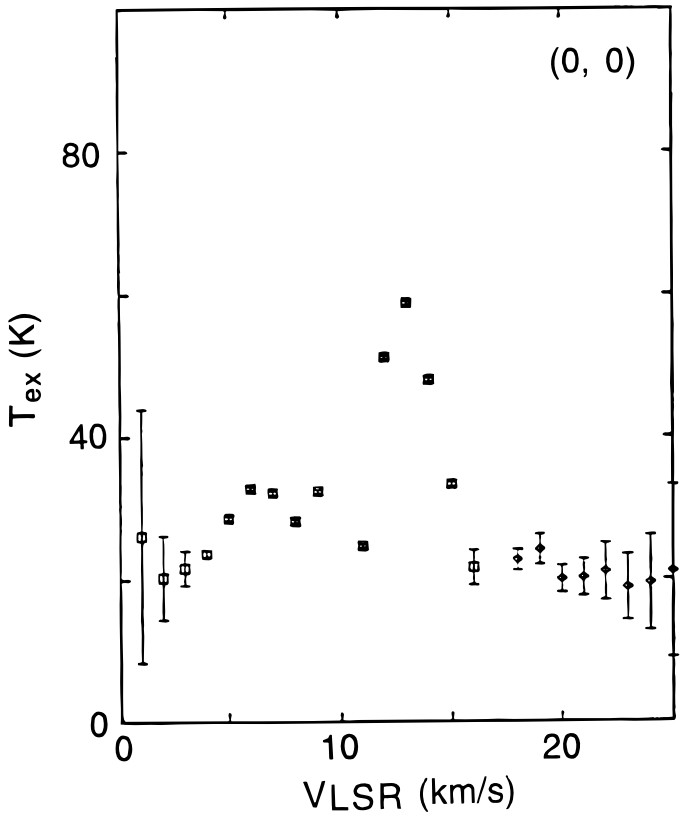

FIG. 6.—Excitation temperature of CO as a function of v_{LSR} at the position of IRS 3. The plotted squares show T_{ex} for velocities at which ^{13}CO is detectable, calculated from eq. (1). The diamond symbols show T_{ex} for velocities with CO emission but no detectable ^{13}CO, calculated using eq. (3).

that the values of T_{thin} and T_{thick} fit together smoothly. That is, there is no large discontinuity in temperature at the transition velocities between the optically thick and optically thin regimes. This agreement is encouraging because it is consistent with filling factors of unity (but does not prove it).

It is curious that the optical depth at the position of IRS 3 has its maximum near 10 km s^{-1} (Figure 5) while T_{ex} peaks closer to 13 km s^{-1} (Figure 6). The ^{13}CO line shows a slight hump near 13 km s^{-1}, coincident wih the temperature peak of ^{12}CO. This ^{13}CO emission feature may represent a separate physical structure. On the other hand, lines of high-density tracers such as H_2CO and CH_3OH peak at 10 km s^{-1} and have no emission feature at 13 km s^{-1}, so any cloud at 13 km s^{-1} cannot have extremely high density.

The derived values of excitation temperature cover the range from 6 to 60 K. The lowest temperatures are found only for the highest velocity gas in several positions. Gas warmer than 45 K is found for the lowest velocity gas toward several CO peaks that may contain embedded sources. For most of the velocity range at most positions, the excitation temperature lies between 20 and 40 K. These temperatures are in general agreement with estimates from ammonia: Montalbán et al. (1990) and Torrelles et al. (1990) found a kinetic temperature between 20 and 30 K on average in the cloud core, and temperatures greater than 45 K toward the position of embedded infrared sources.

4.3. *Column Density and Mass*

When optical depths are known, the CO column density integrated over some velocity range is obtained from

$$N_{tot} = \int 8.0 \times 10^{13} \, [T_{ex}(v) + 0.92] e^{-16.59/T_{ex}(v)} \times (1 - e^{-16.59/T_{ex}(v)})^{-1} \tau_v^{12} \, dv \, , \quad (4)$$

where N_{tot} is in units of cm^{-2} and the velocity units are km s^{-1}. In the optically thin limit, the CO column density is given by

$$N_{tot} = \int 4.6 \times 10^{12} T_{ex}(v) e^{33.2/T_{ex}(v)} T_R^{3\to 2}(v) dv \, . \quad (5)$$

As an example, the column density per unit velocity interval is presented in Figure 7 for the position of IRS 3.

Obtaining reliable total column densities over all velocities is complicated by the fact that some of the intensity peaks can be identified at redshifted and blueshifted velocities but are not visible for part of the velocity range near the line center because of self-absorption. It is likely that those clumps which are seen in maps of both receding and approaching gas are present in the intermediate velocities as well. To account for gas in the narrow velocity range near the line center, we interpolate from the values on either side. The resulting total column density is a lower limit, since the column density could be considerably higher at the line center.

In order to calculate the mass of the CO emission structures, it is necessary to combine the size with the total column density. The features, however, are not discrete, bounded objects moving in a vacuum; they are probably denser structures within surrounding, lower density gas. The diameter is not uniquely defined because intensity peaks merge into a fainter background and their size varies

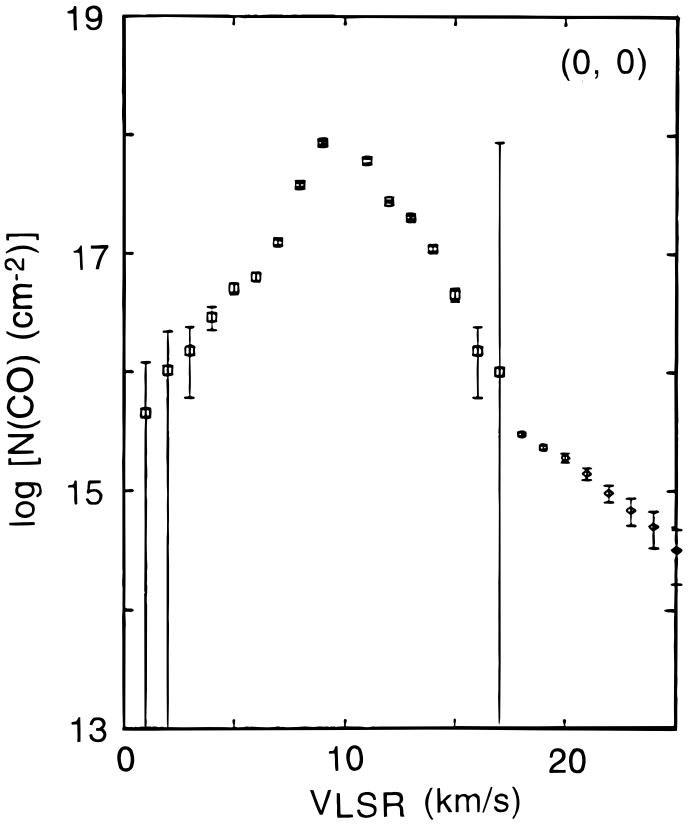

FIG. 7.—CO column density per unit velocity interval toward IRS 3. Results for velocities with calculated optical depth are shown by squares. Results that use the optically thin limit are shown by diamonds.

with velocity. Much of the intensity is concentrated in a 15″ diameter region, so we employ, for simplicity, a diameter of 15″ in each case. Masses of the emission peaks within one beam, presented in Table 2, have values from about 0.1 to 3 $M_\odot$, with the exception of peak 13, which has a lower mass of $\sim 0.01\ M_\odot$. Densities lie in the range 10^4–10^5 cm^{-3}

4.4. *Energetics of the* CO *Emission Peaks*

Because we cannot prove that the intensity maxima are density maxima, we have refrained from calling them clumps. Even so, it is of some interest to examine the consequences if these morphological structures actually are physical clumps, and we do so in this section. A clump contains kinetic energy due to internal gas motions within the clump, observed in the width of spectral lines. A clump may also have kinetic energy of bulk motion of its velocity differs from the mean cloud velocity. We define the bulk velocity of a clump, V_b, as its mass-weighted average velocity, or, equivalently, as the total linear momentum of the clump divided by its mass:

$$V_b = \frac{P_{\rm clump}}{M_{\rm clump}} = \csc 45^\circ \frac{\sum_j m_j(v_j)(v_j - v_0)}{\sum_j m_j(v_j)}, \quad (6)$$

where the v_j is the observed LSR radial velocity of channel j and v_0 is the radial velocity of the cloud. The csc 45° term is the factor by which, on average, the space velocity exceeds the radial velocity. The total bulk kinetic energy is given by $E_{k\text{-}b} = \frac{1}{2} \times M_{\rm clump} \times V_b^2$. The internal kinetic energy of the clump is given by

$$E_{k\text{-in}} = \sum_j \{\tfrac{1}{2} m_j(v_j)(v_j - v_0 - V_b)^2\}, \quad (7)$$

where the sum is over the velocities for which the clump is detectable. Values of bulk velocity, bulk kinetic energy, and internal kinetic energy are given in Table 2.

To determine whether or not the clumps are gravitationally bound, we compare the internal kinetic energy with the gravitational binding energy, $E_{\rm grav}$, where

$$E_{\rm grav} = -\frac{3}{5} \frac{GM_{\rm clump}^2}{R_{\rm clump}}. \quad (8)$$

The value of the gravitational energy of each clump is given in Table 2. It can be seen from Table 2 that the internal kinetic energy is larger than the gravitational energy by at least 1 order of magnitude, a clear indication that the structures are not gravitationally bound. This does not, however, preclude the possibility that the clumps are bound by other mechanisms. For example, ram pressure due to a fast neutral wind could, in principle, confine a clump (Gaden et al. 1991). We do not pursue this possibility because there is no evidence for a directed wind in the Mon R2 core.

The mean lifetime of a clump against dissipation due to expansion can also be calculated. We may first assume that disturbances propagate at the speed of sound, v_s, where $v_s^2 = P_0/\rho$. For $T = 40$ K, the sound speed is 0.3 km s^{-1}, and the time for a pressure wave to move through a 0.06 pc diameter clump is $\sim 2 \times 10^5$ yr. This time is a measure of the lifetime of a clump in the absence of any external confining pressure. Because of the ubiquitous magnetic fields, a more likely signal propagation speed is the Alfvén speed, $v_{\rm A} \approx 2$ km s^{-1} (Shull & Draine 1987), implying a clump lifetime of only 3×10^4 yr.

The very extended CO outflow is evidence that large quantities of kinetic energy have been injected into the cloud core over timescales of 10^5 yr. In § 3 we argued that the source of the extended outflow is now inactive. A new outflow source appears to be emerging, however, namely, IRS 3. The exceptionally high velocity gas in the gas associated with IRS 3 (peak 1 in Table 1) strongly suggests that IRS 3 is the source of a compact outflow, unresolved by our beam. The beam numbered 13 is particularly interesting in this regard because its position varies with velocity (see the channel maps from 23 to 28 km s^{-1} in Fig. 3). The channel map centered at 22 km s^{-1} shows a bridge of gas connecting IRS 3 with peak 13. This peak may well be a stream of gas accelerated by the outflow from IRS 3. Further evidence

TABLE 2

MASSES AND ENERGETICS OF THE CO EMISSION PEAKS

Clump	$M_{\rm clump}$ ($M_\odot$)	V_b (km s^{-1})	$E_{k\text{-}b}$ (ergs)	$E_{k\text{-in}}$ (ergs)	$E_{\rm grav}$ (ergs)
1.....	2.3	−0.4	3.5E42	1.0E44	9.4E42
2.....	2.7	0.05	6.8E40	1.9E44	1.3E43
3.....	2.4	−0.6	9.1E42	2.0E44	9.6E42
4.....	1.7	−2.8	1.3E44	7.7E43	4.7E42
5.....	2.3	−0.8	1.3E43	1.4E44	9.2E42
6.....	2.5	−0.6	1.0E43	1.6E44	1.1E43
7.....	0.08	−4.9	1.8E43	4.9E41	9.7E39
8.....	0.85	−2.9	7.4E43	3.5E43	1.3E42
9.....	0.18	−4.2	3.1E43	2.2E42	5.3E40
10.....	0.17	7.7	1.0E44	4.9E42	5.1E40
11.....	0.09	7.5	5.3E43	4.0E42	1.5E40
12.....	0.12	10.2	1.2E44	3.0E42	2.3E40
13.....	0.007	14.6	1.6E43	3.0E41	9.2E37

for a compact outflow from IRS 3 is provided by the detection of blueshifted CO in absorption, discussed in § 6 below.

5. THE DISTRIBUTION OF DENSE GAS: HCN AND H_2CO

Figure 8 is a map of the integrated intensity of HCN $J = 4$–3 emission. The highest intensity HCN emission is organized around a circular region of low intensity. The central "hole" coincides in position and size with the compact H II region. The most intense emission is from a clump of gas associated with IRS 3. A second arc of intense emission lies to the southwest, centered at $(-50'', -20'')$. Emission extends to the north and west from IRS 3. Figure 9 shows the integrated intensity of H_2CO ($5_{1,5}$–$4_{1,4}$) emission. The H_2CO map is generally similar to the HCN map, with the strongest peak at IRS 3, a region of strong emission to the southwest, and an extension to the north and west from IRS 3. A major difference is that formaldehyde has an intensity peak to the north, where HCN has only relatively weak emission. This difference might be due to excitation or to a difference in the relative abundances of H_2CO and HCN. We cannot distinguish between these possibilities without data on other transitions of the molecules.

The peak velocity of the H_2CO line varies systematically by about 2 km s^{-1} across the mapped region. This is seen in Figure 10, where blueshifted gas (velocity 5–10 km s^{-1}) and redshifted gas (velocity 10–15 km s^{-1}) are shown separately. The distribution of gas has the appearance of an outflow from IRS 3. This however, is not the case. We are not seeing red and blue line wings that vary systematically with position. Rather, the line peak is varying with position. Gas associated with IRS 3 has larger H_2CO (and HCN) line widths than gas elsewhere, so that IRS 3 shows strong emission in both the red and blue maps. The larger line widths at IRS 3 may well be due to a compact outflow from IRS 3, but higher angular resolution will be needed to study its morphology. The most plausible interpretation of the

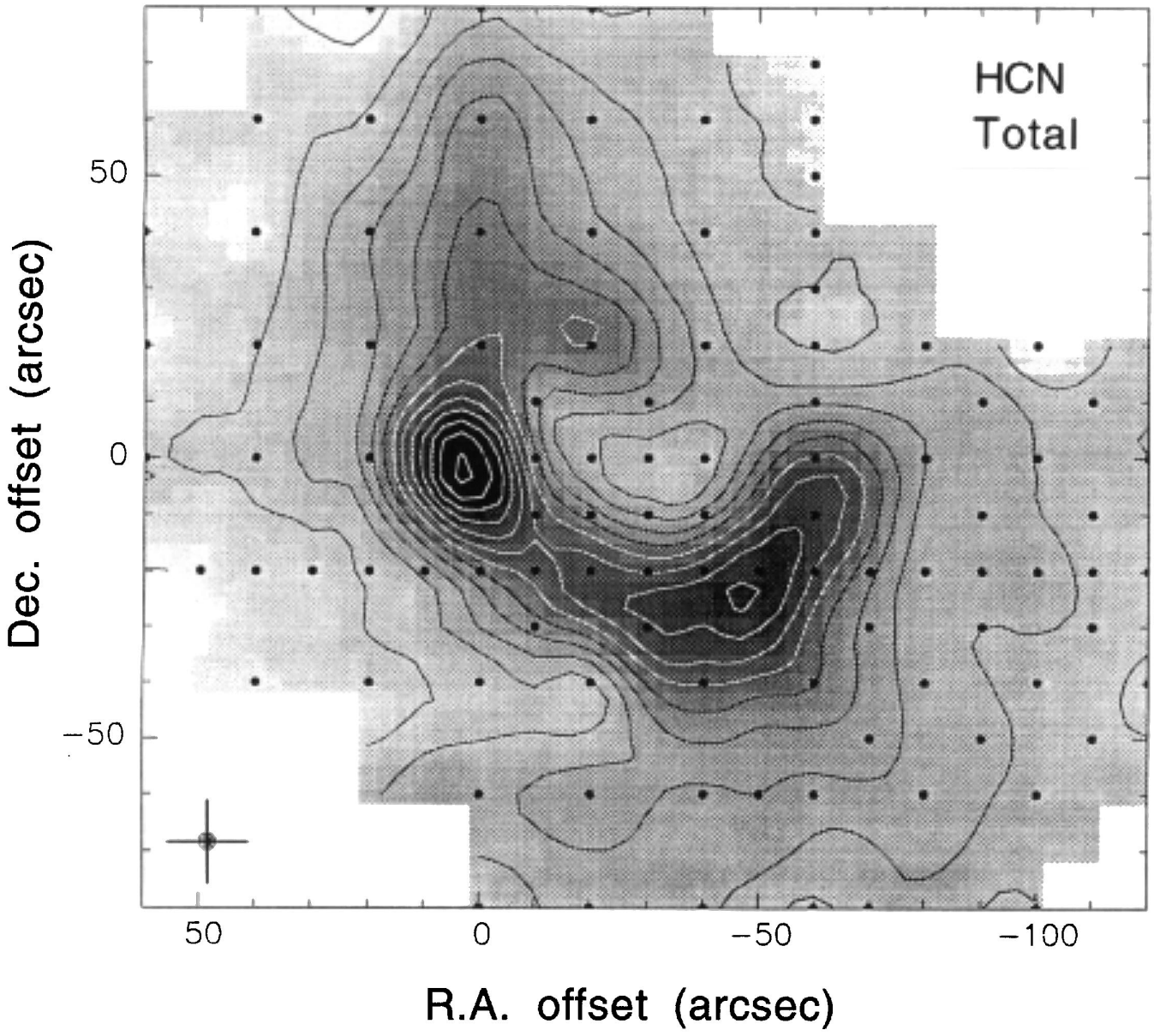

FIG. 8.—Integrated intensity map of HCN $J = 4$–3 emission. The lowest contour level shown is 3.6 K km s^{-1}, and the interval between contours is 3.6 K km s^{-1}. Observed positions are shown by filled circles.

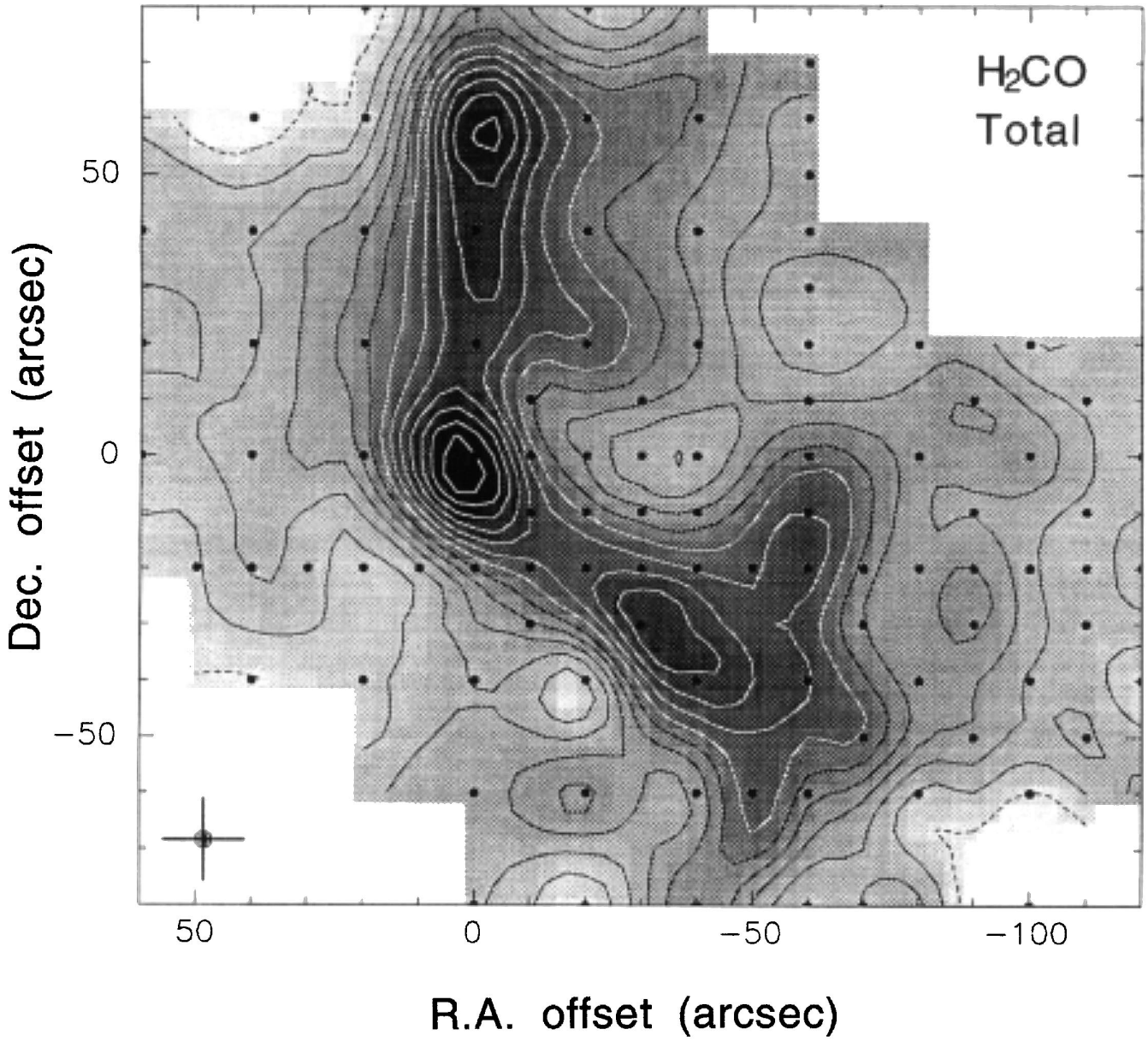

FIG. 9.—Integrated intensity map of H_2CO ($5_{1,5}$–$4_{1,4}$) emission. The lowest contour is -0.7 K km s^{-1}, and the interval between contours is 0.7 K km s^{-1}. Observed positions are shown by filled circles.

H_2CO and HCN data is that the central region of Mon R2 possesses three main concentrations of dense gas moving at 1 or 2 km s^{-1} with respect to each other. These are the clump containing IRS 3, the complex region to the southwest, and the emission region to the north. Despite the apparent bridges of emission connecting these three regions, they may not be physically connected. In fact, Hodapp (1987) has argued, on the basis of the polarization of 2.2 μm radiation, that IRS 3 cannot be close to the dust shell that surrounds the compact H II region, but must be separated from this shell by a considerable distance ($\geq$0.6 pc) along the line of sight.

The HCN and H_2CO integrated intensity maps (Figs. 8 and 9) are generally similar to the CO $J = 3$–2 integrated intensity map (Fig. 2). All three molecules show peaks to the east (IRS 3), the southwest, and the north, surrounding a central minimum. This agreement suggests that the CO emission is tracing even the densest gas, something that is not expected. The $J = 3$–2 transition of CO can be excited at gas densities of $\sim 10^4$ cm^{-3} (in the optically thin limit), as opposed to the density of $\sim 10^6$ cm^{-3} required for the HCN and H_2CO emission. The lower density required for excitation, together with the high abundance of CO, might be expected to preclude the detection of the densest gas by CO emission. But CO is an unexpectedly good tracer of the dense inner structure of the Mon R2 cloud because of the large velocity dispersion of the gas in the core. As demonstrated by the calculations of the previous section, only at velocities near the two absorption features (7.6 and 11.3 km s^{-1}) does high optical depth prevent the determination of a reliable CO column density.

We note that a high-resolution (10″) map of the inner 3′ × 3′ of Mon R2 in HCO^+ $J = 1$–0 (Gonatas et al. 1992) is significantly different from our HCN and H_2CO maps. The HCO^+ map has a relative minimum to the southeast of the central hole rather than to the northwest. Another difference is the absence of an emission peak at IRS 3. We believe that the self-absorption in this optically thick line

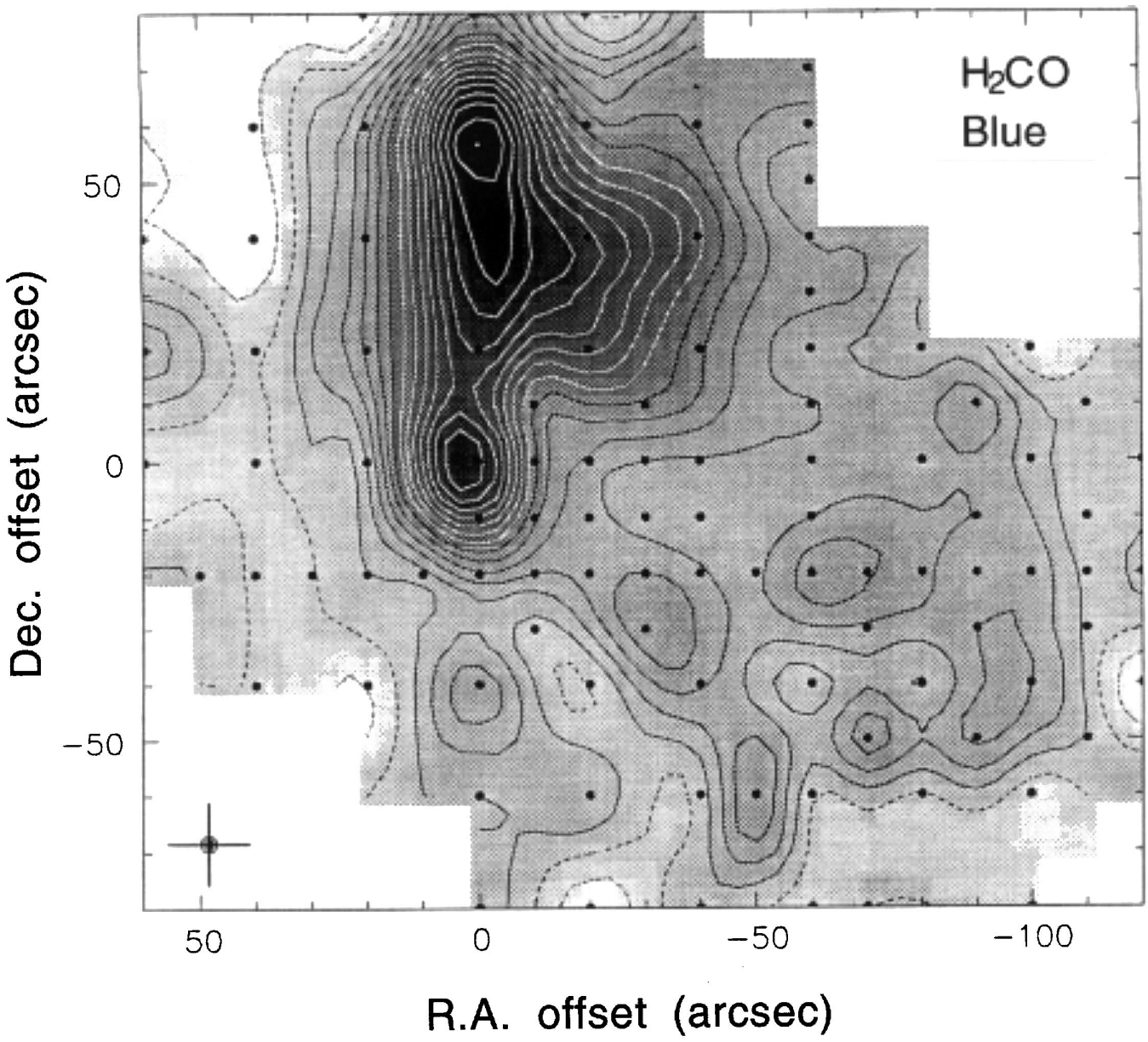

FIG. 10.—Integrated intensity maps of H_2CO ($5_{1,5}$–$4_{1,4}$) emission for velocities in the range 5 km s^{-1} < v_{LSR} < 10 km s^{-1} (blue) and velocities in the range 10 km s^{-1} < v_{LSR} < 15 km s^{-1} (red).

(see Gonatas et al., Fig. 4) makes it a poor tracer of the dense, inner, warm gas.

6. RESULTS FROM THE INFRARED SPECTRUM OF IRS 3

Characteristics of the *M*-band spectrum have been given in § 2. A great advantage of broadband infrared spectroscopy over millimeter heterodyne spectroscopy is the ability to acquire many lines simultaneously. The filter passband was selected to include much of the fundamental band[3] of CO. Strong CO absorption lines at the cloud core velocity are seen throughout the spectrum (specifically *P*14 through *R*8), but they are saturated and are not useful for the calculation of gas properties. Lines of ^{13}CO are also present (*P*4 through *R*15). The ^{13}CO lines are not saturated and can be used to calculate temperature and column densities.

Two portions of the complete spectrum are shown in Figure 11. The spectrum shown is the ratioed spectrum, in which the spectrum of IRS 3 has been divided by a spectrum of the Moon to remove telluric lines. Two ^{12}CO lines, *P*8 and *P*7, are labeled in the figure. The lines have two velocity components: The stronger (to the left) has the velocity of the cloud core ($\sim$10 km s^{-1}) while the other is blueshifted by 9 km s^{-1}. Four ^{13}CO lines are present in Figure 11, namely the *R*3, *R*4, *R*12, and *R*13 lines. The ^{13}CO lines have only a single component at the same velocity as the stronger ^{12}CO feature. The absence of a blueshifted velocity component in ^{13}CO corresponding to the blueshifted ^{12}CO component implies that the blueshifted ^{12}CO component has only moderate optical depth. Unfortunately, the two CO velocity components are blended, making measured equivalent

[3] The fundamental absorption band is formed when CO molecules in the ground vibrational state are raised to the first excited vibrational state by the absorption of infrared (4.6 μm) photons. The transitions ($v = 0, J$) to ($v = 1, J + 1$) constitute the *R* branch of the fundamental band; transitions ($0, J$) to ($1, J - 1$) comprise the *P* branch.

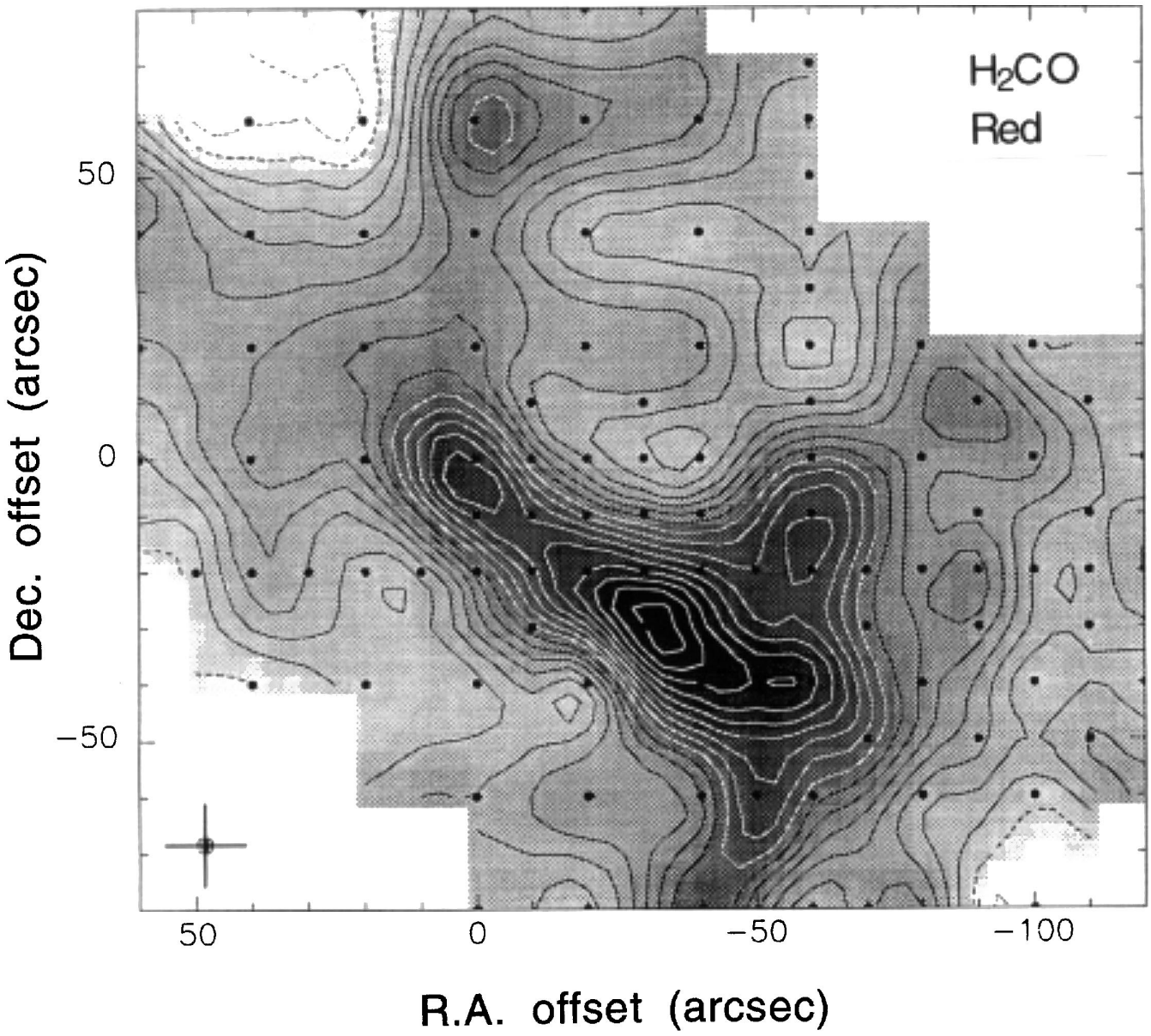

FIG. 10—*Continued*

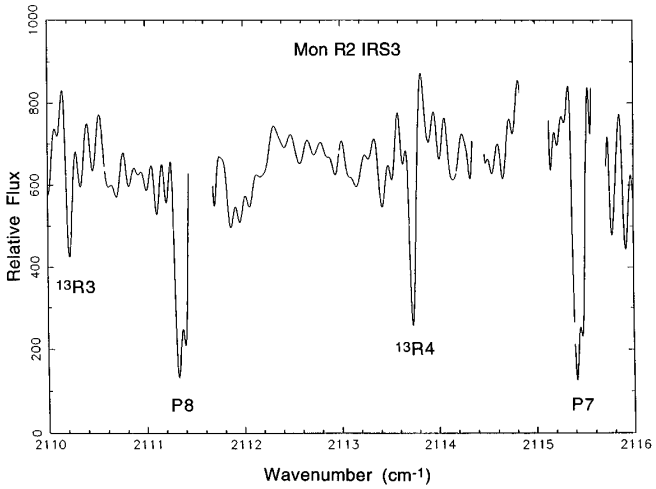

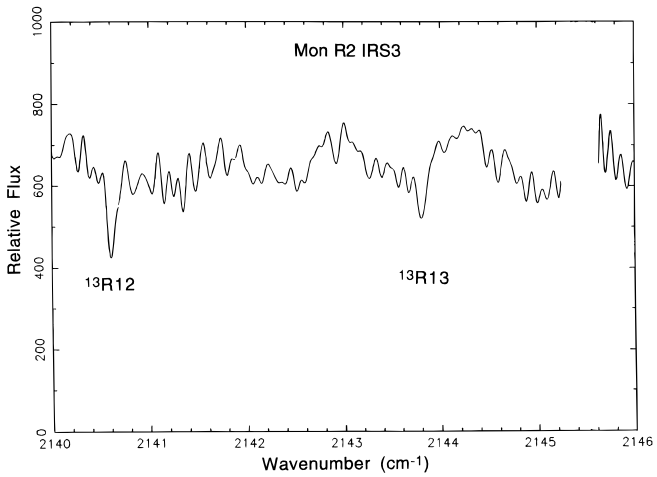

FIG. 11.—Two portions of the *M*-band spectrum of IRS 3, after division by the spectrum of the Moon to remove telluric lines. The *P*7 and *P*8 lines of ^{12}CO and the *R*3, *R*4, *R*12, and *R*13 lines of ^{13}CO are labeled. Gaps in the spectrum indicate the positions of saturated telluric lines which produce spikes in the ratioed spectrum.

widths of the blueshifted feature very uncertain. The presence of the 9 km s^{-1} absorption feature out to $J = 14$, the limit of the bandpass, implies that the gas is hot, at least several hundred kelvins. The absence of a corresponding emission feature in the CO $J = 3$–2 spectrum at the position of IRS 3 means that the outflowing gas occupies an area much smaller than the 14″ beam of the CO $J = 3$–2 observations. We may be seeing evidence in the 9 km s^{-1} feature of a recent outburst from IRS 3.

The method of analysis of the spectral lines follows that of Mitchell et al. (1989, 1990), where examples of M-band spectra of other embedded young stellar objects can be found. For each line, the column density of ^{13}CO in the initial rotational state is calculated using a curve-of-growth analysis. An intrinsic line width of 3.5 km s^{-1} is used. This is found by correcting the observed average line width for the instrumental width of 5.2 km s^{-1}. The results are given in Table 3. The columns of Table 3 show, for each absorption line, the line designation, the energy of the initial state in temperature units, the observed equivalent width, the optical depth at line center from the curve-of-growth analysis, and the column density of ^{13}CO in the initial rotational state of the transition.

If the CO is in thermodynamic equilibrium, the rotational level populations will follow the Boltzmann equation, and $N_J/(2J + 1) \propto \exp(-E_J/kT)$. It is, therefore, useful to plot $\ln[N_J/(2J + 1)]$ versus E_J/k: if the points fall on a straight line, then thermodynamic equilbrium is probably a valid assumption and the line slope yields the gas temperature. Figure 12 shows such a Boltzmann plot. It is clear that a single straight line is a poor representation of the data. The distribution of points shows a break at $E_J/k \approx 100$ K. The low-J points can be fitted by one straight line, while the higher J points can be fitted by a second line of shallower slope. Our interpretation, as made previously for other embedded sources (e.g., Mitchell et al. 1990), is that the low-J lines are formed in cold gas, while the high-J lines are formed in hot gas. The lines in Figure 12 are least-squares fits. The colder gas has $T = 45^{+12}_{-8}$ K, where the uncertainties are 1 standard deviation. This temperature is consistent with temperatures deduced from emission lines. We take it to represent the temperature of the clump of dense gas surrounding IRS 3 which is seen in the CO, HCN,

TABLE 3

^{13}CO $v = 0$–1 Absorption Lines in the Spectrum of Mon R2 IRS 3

Line	E_J/k (K)	W[a] (cm^{-1})	τ_0[b]	N_J[c] (cm^{-2})
P4	52.9	0.031	1.3	7.3E15
P3	31.7	0.040	4.4	2.7E16
P2	15.9	0.039	4.1	2.6E16
P1	5.3	0.027	1.8	1.4E16
R2	15.9	0.037	3.4	1.5E16
R4	52.9	0.028	1.9	8.6E15
R5	79.3	0.035	3.0	1.4E16
R9	238	0.022	1.2	6.0E15
R10.....	291	0.021	1.2	5.6E15
R11.....	349	0.019	0.98	4.8E15
R12.....	412	0.016	0.77	3.8E15
R13.....	481	0.014	0.65	3.2E15
R15.....	634	0.014	0.65	3.2E15

[a] Equivalent width of the line.
[b] Optical depth at line center.
[c] Column density of CO in rotational state J.

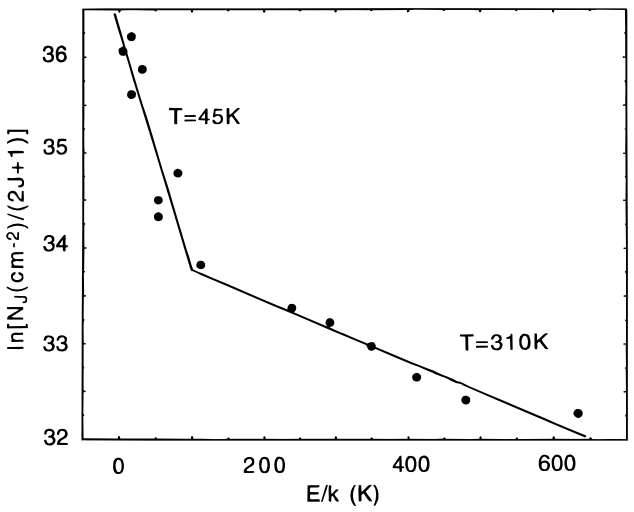

Fig. 12.—Excitation diagram for ^{13}CO toward Mon R2 IRS 3. Column densities in each rotational sublevel are plotted as a function of the rotational energy in kelvins. LTE excitation temperatures are obtained from separate least-squares fits to the low-J lines (45 K) and the high-J lines (310 K).

ad H_2CO maps presented in previous sections. The hot gas, with $T = 310^{+34}_{-30}$ K is probably gas very close to IRS 3 and heated by its radiation. The absence of evidence for the hot gas in the emission-line data is not surprising because the hot gas is likely to be subarcsecond in size, so that beam-filling factors are small.

The column density of ^{13}CO is found for each temperature component as follows: Using the partition function at the appropriate temperature, the total ^{13}CO column density is calculated from each N_J of Table 3. The mean and standard deviation are found from this set. We find a ^{13}CO column density of $(9.0 \pm 3.3) \times 10^{16}$ cm^{-2} for the 45 K gas and $(7.4 \pm 0.9) \times 10^{16}$ cm^{-2} for the 310 K gas. If we assume that IRS 3 lies at the center of its surrounding gas clump, the total column density is twice the foreground column density, so that $N(^{13}CO) = 1.8 \times 10^{17}$ cm^{-2} for the 45 K gas. To convert the ^{13}CO column density to a ^{12}CO column density, we adopt an abundance ratio $^{12}CO/^{13}CO = 60$, to find $N(^{12}CO) = (1.1 \pm 0.4) \times 10^{19}$ cm^{-2}. The CO column density at the position of IRS 3, deduced from CO emission lines following methods outlined in § 4, is $(3.7 \pm 0.5) \times 10^{18}$ cm^{-2}. The quoted error is due entirely to noise in the data. The fact that the column density from CO emission lines is a factor of 3 lower than that found from the ^{13}CO absorption-line analysis is almost certainly due to the high and uncertain optical depth at the emission-line core. In view of the discrepancy for IRS 3, the masses given in Table 2 should be interpreted as lower limits.

7. MILLIMETER AND SUBMILLIMETER CONTINUUM MAPS

Figure 13 shows the continuum maps at 450, 800, 1100 and 1300 μm. The beamwidths (FWHP), shown as filled circles on each map, are 14″ for the 450 and 800 μm maps, 20″ for the 1100 μm map, and 25″ for the 1300 μm map.

The two shortest wavelength maps are similar, consisting of numerous emission peaks embedded in fainter background emission. The general form is a bar, oriented northeast to southwest, with extensions from either end of the bar. The 1100 μm and 1300 μm maps are quite different, consisting of a dominant central peak surrounded by a

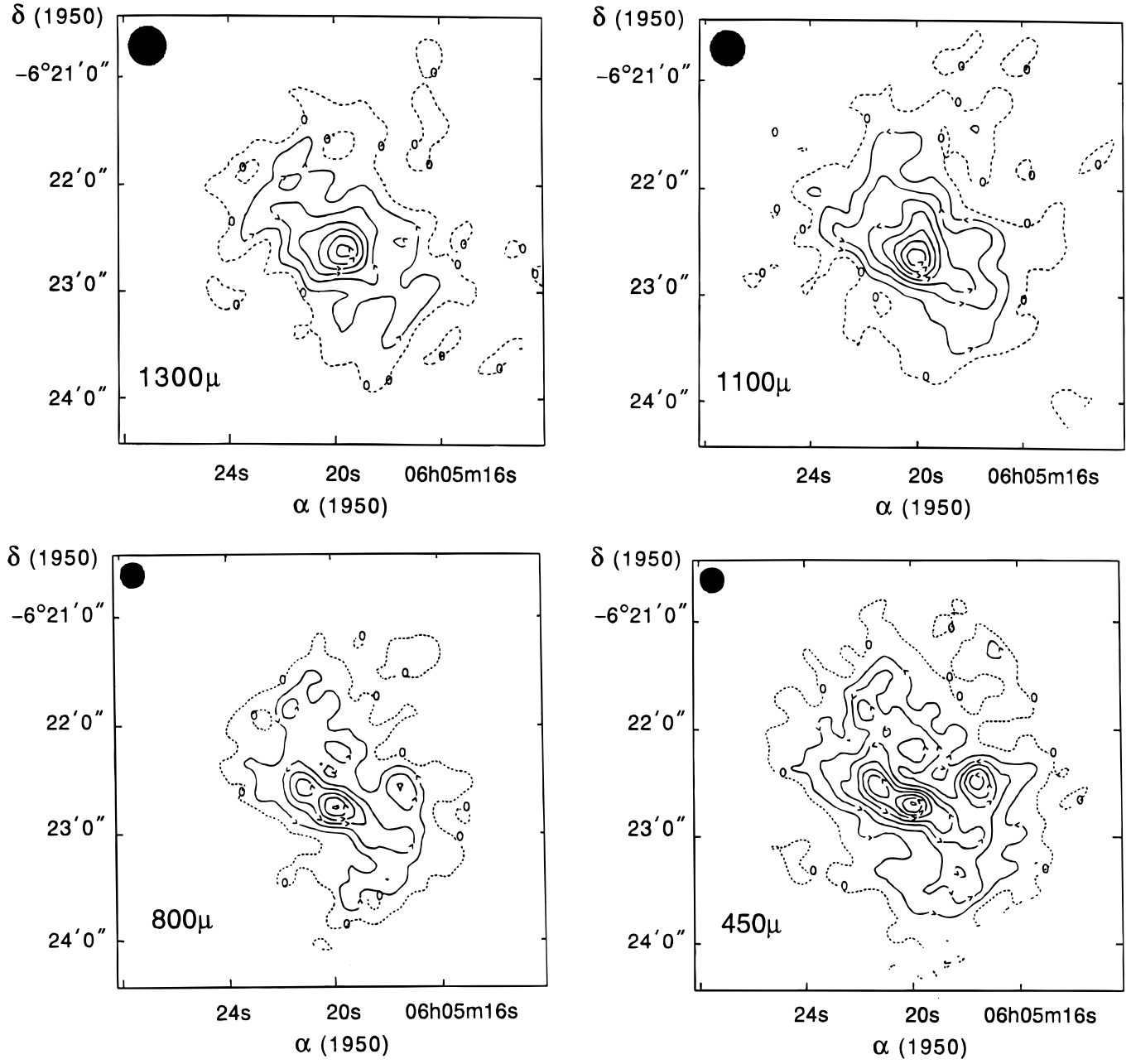

FIG. 13.—Continuum maps of Mon R2 at 1300, 1100, 800, and 450 μm. In the 1300 and 1100 μm maps, the lowest contour (*dashed line*) is 0.5 Jy beam^{-1} and the contour interval is 0.5 Jy beam^{-1}. In the 800 μm map, the lowest contour is 1 Jy beam^{-1} and the contour interval is 1 Jy beam^{-1}. In the 800 μm map, the lowest contour is 1 Jy beam^{-1} and the contour interval is 1 Jy beam^{-1}. In the 450 μm map, the lowest contour is 5 Jy beam^{-1} and the contour interval is 5 Jy beam^{-1}.

fainter envelope. The morphology of the longer wavelength maps suggests that free-free emission from the H II region makes a dominant contribution to the observed flux. In the following, we use only the shorter wavelength maps to determine dust mass.

We have used the 800 μm map to identify intensity peaks. Hereafter we will refer to these peaks as clumps on the assumption that they are density peaks, but it should be kept in mind that temperature enhancements can also give rise to intensity maxima. We find eleven clumps, labeled C1–C11 in Figure 14. Also shown in Figure 14 are infrared sources from Aspin & Walter (1990) that are close to a clump and may be embedded within it. From a 1300 μm map with 11″ resolution, Henning, Chini, & Pfau (1992) found seven clumps. Six of their seven clumps are confirmed here. Their clump 4 was inferred from a northern extension of the 1300 μm emission and was claimed to be associated with IRS 2. We find no 800 μm peak associated with IRS 2. In fact IRS 2 is at a relatively low-intensity region northwest of IRS 1. The higher intensity of emission from the region just north of IRS 1, seen at longer wavelengths, is possibly due to free-free emission from the H II region. At 800 μm (and below), free-free emission will be negligible and emission from cold dust will be more intense. Table 4 lists the eleven clumps, the equivalent sources from Henning et al. (1992), the infrared sources that may be associated with them and the clump masses (discussed below).

A comparison of the continuum maps, which trace dust, and the molecular maps, which (of course) trace gas, is of great interest. When the HCN and H_2CO integrated inten-

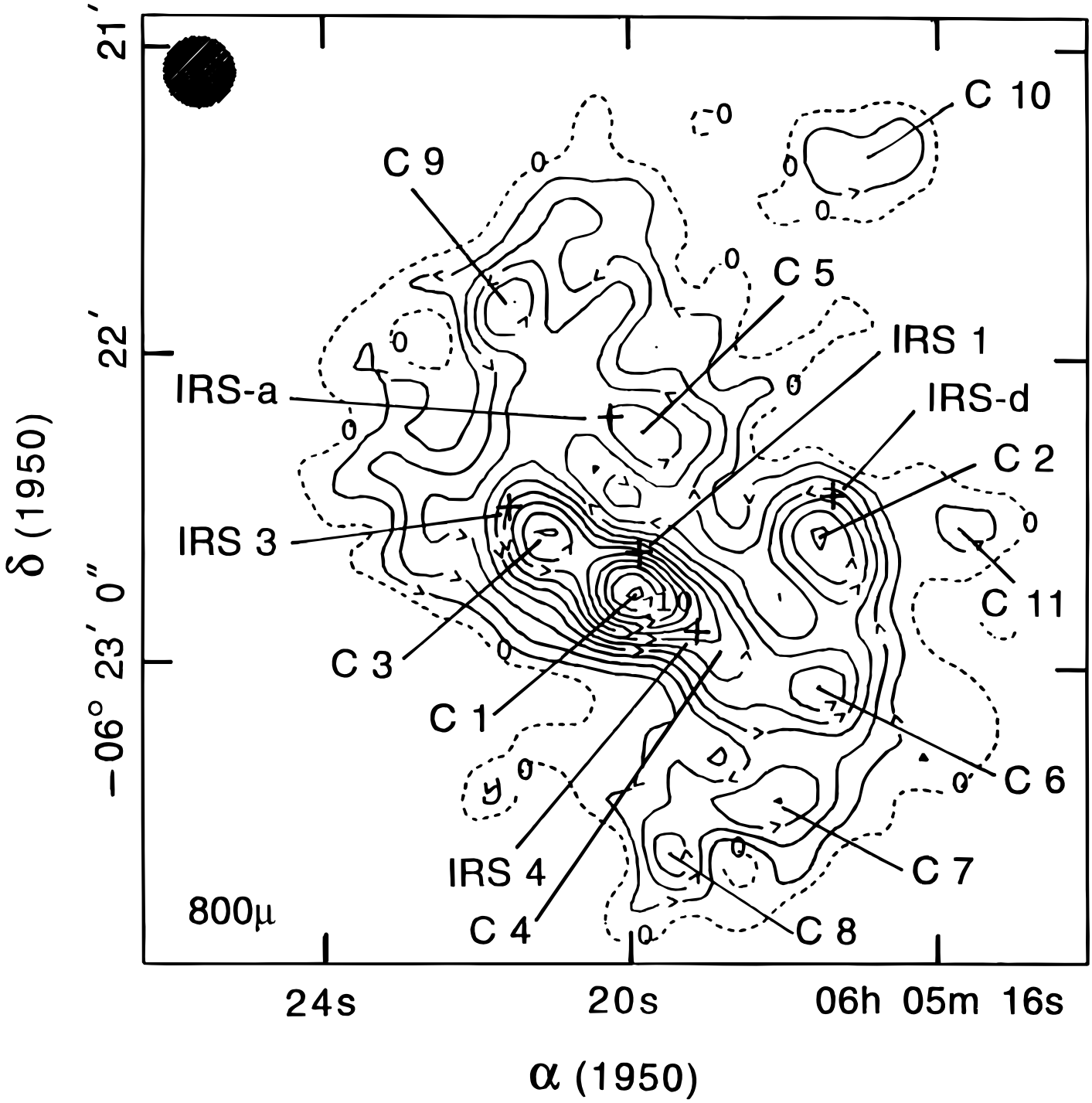

FIG. 14.—Same 800 μm map as shown in Fig. 13, but with the lowest contour level of 1 Jy beam^{-1} and a contour interval of 0.5 Jy beam^{-1}. The continuum peaks are labeled C1–C11. The plus signs indicate five 2 μm sources from Aspin & Walter (1990), which are close to a continuum clump and may be physically associated with it.

sity maps (Figs. 8 and 9) are compared with the 800 μm continuum map, the first impression is that the dust and gas maps are rather different. It is evident, however, that most of the difference is due to the dominance of the central continuum clump, C1. In the molecular maps there is no peak at the position of C1, just a connecting bridge of emission. Except for this central emission peak, features in the continuum and molecular maps show a close correspondence. A strong emission peak is present at IRS 3 in both, both have an extension to the north with a branch to the west, and both have an arc of emission in the southwest.

How are we to understand the prominence of clump C1 in the continuum? The answer lies with the compact H II region. Continuum clump C1 coincides with the the bright arc of radio emission at the southern edge of the H II region (Massi et al. 1985). A Brα $n = 5$–4 (4.052 μm) image (Howard et al. 1994) is essentially identical to the radio continuum image. The emission arc has been interpreted as

TABLE 4

POSITIONS AND MASSES OF CONTINUUM PEAKS

Peak Name	Offsets from IRS 3	Mass ($M_\odot$)[a]	Clump Number[b]	2 μm Source[c]
C1	−24, −20	12.2	5	IRS 1
C2	−60, −8	7.0	2	IRS d
C3	−5, −8	9.5	6	IRS 3
C4	−41, −31	6.0	3	IRS 4
C5	−25, +12	5.2	4	IRS a
C6	−60, −38	6.0	1	...
C7	−51, −59	5.2	...	...
C8	−31, −70	4.3	...	...
C9	0, +37	6.0	7	...
C10.....	−65, +67	2.6	...	...
C11.....	−87, −7	2.6	...	...

[a] Calculated using $T_{\rm dust} = 45$ K in each case.
[b] Numbering of Henning et al. 1992.
[c] From Aspin & Walter 1990.

a dense ionization front propagating into foreground dense molecular gas. Dust within and behind the ionization front will be heated, emitting strong continuum radiation. Molecules, on the other hand, will be destroyed in the H II region, leading to a deficiency in molecular emission, as observed.

To determine clump masses, we assume optically thin emission, so that the mass of dust is

$$M_d = \frac{F_\nu d^2}{\kappa_\nu B_\nu(T_d)}, \tag{9}$$

where F_ν is the flux, d is the distance, T_d is the dust temperature, and κ_ν is the mass absorption coefficient in cm^2 g^{-1}. We assume a power law, $\kappa_\nu \propto \nu^\beta$ and follow Hildebrand (1983) in using a value of 10 cm^2 g^{-1} for κ_ν at 250 μm. Then, for a gas-to-dust ratio of 100, the gas mass can be written (Zinnecker et al. 1992)

$$M_{\rm gas}(M_\odot) = 0.019 F_\lambda \left[\frac{\lambda({\rm mm})}{0.25}\right]^{\beta+3} (e^{14.4/\lambda({\rm mm})T_d} - 1) d^2 \tag{10}$$

Here, F_λ is the flux in janskys, T_d is the dust temperature in kelvins, and d is the source distance in kiloparsecs. We adopt a dust temperature of 45 K, in agreement with the gas temperature found for the gas in the line of sight to IRS 3 (§ 6), and consistent with the dust temperature of 50 K found from far-infrared emission by Thronson et al. (1980). The value of β is uncertain: $\beta = 2$ is often used in the submillimeter region, although $\beta = 1.5$ is sometimes adopted. With observed fluxes at two wavelengths, it is possible to calculate β, for any T_d, using

$$\frac{F_1}{F_2} = \left(\frac{\lambda_1}{\lambda_2}\right)^{-\beta} \frac{B_{\lambda_1}(T_d)}{B_{\lambda_2}(T_d)}. \tag{11}$$

Applying equation (11) to the 800 and 450 μm fluxes from clump C2, and using $T_d = 45$ K, we find $\beta = 1.8$. Henning et al. (1992) used 870 and 1300 μm fluxes to find $\beta = 1.3$, considerably smaller than expected. As an explanation, they suggest that the source diameter may increase with wavelength. Another possibility is that the 1300 μm flux is affected by free-free emission from the H II region.

The calculated clump masses for $\beta = 1.8$ and $T_d = 45$ K are given in Table 4. The masses range from 3 to 12 $M_\odot$. For the six clumps in common with Henning et al. (1992), we find masses lower than those of Henning et al. by factors between 2 and 4. Only a small part of this difference can be due to different assumptions about grain emission properties. We entered their 1300 μm flux for clump C3 (their clump 6) and their adopted $T_d = 50$ K in equation (10) to find a mass of 22.4 $M_\odot$, not very different from their tabulated mass of 27.3 $M_\odot$. The larger masses of Henning et al. may be due, in part to free-free emission contributing to the 1300 μm flux. This suggestion receives some support from the fact that the discrepancy is largest (a factor of 3.7) for clump C1, which is centered on the H II region, and is smallest for C9, which is the farthest from the H II region (of Henning et al.'s clumps).

If the clump C1 is, in fact, inside the H II region, it will be heated by radiation from IRS 1 and so the mass given in Table 4 (which employs a dust temperature of 45 K) will be an overestimate. We here calculate the dust temperature, applying the condition of balance between absorbed and emitted radiation and assuming no extinction between IRS 1 and C1. IRS 1 is estimated to be a B0 star (Downes et al. 1975), so we use $T_{\rm eff} = 30{,}000$ K and $R = 7\ R_\odot$. The projected distance between C1 from IRS 1 is $\sim 5''$, or 0.02 pc. The resulting temperature depends on the actual separation and on the frequency dependence of dust absorption, described by the index β. We present results for $\beta = 1$ and $\beta = 2$ and for two values of the separation. If the clump C1 is 0.02 pc (0.06 pc) from IRS 1 and $\beta = 1$, the dust equilibrium temperature is 200 K (130 K). For the same distances but $\beta = 2$, the dust temperature is 450 K (310 K). With such high temperatures, the mass of C1 would be lower by a factor of 2–4 and C1 would no longer be the most massive dust clump in the Mon R2 core.

8. CONCLUSION

1. A map of the inner 3′ of the Mon R2 cloud in CO $J = 3$–2 emission shows numerous intensity peaks. We have calculated the mass within a beamwidth toward each peak and find that lower limits to their masses lie in the range 0.1–3 $M_\odot$. Because we lack values for the excitation temperature across the map, we are unable to distinguish between temperature maxima and density maxima (i.e., clumps) for the CO peaks. If interpreted as clumps, they have such large internal velocity dispersion that they cannot be confined by gravity.

2. Velocity channel maps do not show an obvious bipolar distribution for the brightest CO-emitting gas, suggesting that the source of the very extended Mon R2 bipolar outflow is now inactive. On the other hand, widespread, diffuse gas does show a general bipolar distribution consistent with the extended outflow, but no collimated structures point to a particular source.

3. The gas surrounding IRS 3 shows the highest velocities (CO line width of 75 km s^{-1}), suggesting the presence of a compact, unresolved outflow from IRS 3. A bridge of gas 1′ in length connects IRS 3 with a redshifted CO peak (clump 13 in Fig. 3), which may be a stream of gas accelerated by the outflow. Fundamental band absorption lines of CO show a velocity component which is blueshifted by 9 km s^{-1} relative to the rest-velocity gas, providing further evidence for a compact outflow from IRS 3.

4. Maps in H_2CO ($5_{1,5}$–$4_{1,4}$) and HCN (4–3) emission show that much of the dense gas is distributed in three structures with different velocities. The northern feature is more prominent in H_2CO than in HCN, but we have insuf-

ficient data to determine whether this reflects an abundance difference or a difference in excitation conditions.

5. Fundamental band absorption lines of ^{13}CO are used to obtain the temperature and column density of gas toward IRS 3. Gas with two different temperatures (45 K and 310 K) is present in the line of sight. We identify the colder gas as a clump surrounding IRS 3 which is detected in H_2CO, HCN, and continuum emission. The hot component is probably gas very close to IRS 3 and heated by its radiation.

6. Maps of continuum emission at 1300, 1100, 800, and 450 μm show a number of intensity peaks. Using the submillimeter maps, which show dust emission uncontaminated by free-free radiation, we identify 11 clumps, with masses in the range 3–10 $M_\odot$. The submillimeter maps are broadly consistent with the morphology seen in HCN and H_2CO except for the prominence of a continuum clump, C1, which lies near the edge of the compact H II region. We interpret this clump as due to dust within the H II region and warmed by IRS 1 to a temperature of 200–400 K.

We thank the staff of the JCMT and CFHT, particularly the telescope operators, for their expert assistance. G. F. M. is grateful for a research grant from the Natural Sciences and Engineering Research Council (NSERC). Lorne Avery kindly obtained the CO (2–1) spectra during a service observing run at the JCMT.

REFERENCES

Aspin, C., & Walter, D. M. 1990, A&A, 235, 387
Bally, J., & Lada, C. 1983, ApJ, 265, 824
Beckwith, S., Evans, N. J., II, Becklin, E. E., & Neugebauer, G. 1976, ApJ, 208, 390
Bevington, P. R. 1969, Data Reduction and Error Analysis for the Physical Sciences (New York: McGraw-Hill)
Downes, D., Winnberg, A., Goss, W. M., & Johansson, L. E. B. 1975, A&A, 44, 243
Duncan, W. D., et al. 1990, MNRAS, 243, 126
Garden, R. P., Hayashi, M., Gatley, I., Hasegawa, T., & Kaifu, N. 1991, ApJ, 374, 540
Gonatas, C. P., Palmer, P., & Novak, G. 1992, ApJ, 398, 118
Haslam, C. G. T. 1974, A&AS, 15, 333
Henning, Th., Chini, R., & Pfau, W. 1992, A&A, 263, 285
Heyer, M. H., Snell, R. L., Goldsmith, P. F., Strom, S. E., & Strom, K. M. 1986, ApJ, 308, 134
Hildebrand, R. H. 1983, QJRAS, 14, 267
Hodapp, K.-W. 1987, A&A, 172, 304
Howard, E. M., Pipher, J. L., & Forrest, W. J. 1994, ApJ, 425, 707
Knapp, G. R., & Brown, R. L. 1976, ApJ, 204, 21
Kutner, M. L., & Tucker, K. D. 1975, ApJ, 199, 79
Langer, W. D., & Penzias, A. A. 1990, ApJ, 357, 477
Linke, R. A., & Goldsmith, P. F. 1990, ApJ, 235, 437
Loren, R. B. 1977, ApJ, 215, 129
Loren, R. B., Peters, W. L., & Vanden Bout, P. A. 1974, ApJ, 194, L103
MacDonald, R. H., Little, L. T., Brown, A. T., Riley, P. W., Mathewson, D. N., & Felli, M. 1981, MNRAS, 195, 387
Mangum, J. G., & Wootten, A. 1993, ApJS, 89, 123
Massi, M., Felli, M., & Simon, M. 1985, A&A, 152, 387
Matthews, H. E. 1992, The James Clerk Maxwell Telescope: A Guide for the Prospective User (University Park: Joint Astronomy Centre)
Meyers-Rice, B. A., & Lada, C. J. 1991, ApJ, 368, 445
Mitchell, G. F., Curry, C., Maillard, J.-P., & Allen, M. 1989, ApJ, 341, 1020
Mitchell, G. F., Maillard, J.-P., Allen, M., Beer, R., & Belcourt, K. 1990, ApJ, 363, 554
Montalbán, J., Bachiller, R., Martín-Pintado, J., Tafalla, M., & Gómez-Gonzalez, J. 1990, A&A, 233, 527
Racine, R., & van den Bergh, S. 1970, in IAU Symp. 38, The Spiral Structure of Our Galaxy, ed. W. Becker & G. Contopoulos (Dordrecht: Reidel), 219
Richardson, K. J., White, G. J., Monteiro, T. S., & Hayashi, S. S. 1988, A&A, 198, 237
Sandell, G. 1994, MNRAS, 271, 75
Shull, J. M., & Draine, B. T. 1987, in Interstellar Processes, ed. D. J. Hollenbach & H. A. Thronson (Dordrecht: Reidel), 283
Tafalla, M., Bachiller, R., & Wright, M. C. H. 1994, ApJ, 432, L127
Thronson, H. A., Gatley, I., Harvey, P. M., Sellgren, K., & Werner, M. W. 1980, ApJ, 237, 66
Torrelles, J. M., Ho, P. T. P., Rodríguez, L. F., & Cantó, J. 1990, ApJ, 349, 529
Torrelles, J. M., Rodríguez, L. F., Cantó, J., Carral, P., Marcaide, J., Moran, J. M., & Ho, P. T. P. 1983, ApJ, 274, 214
van den Bergh, S. 1966, AJ, 71, 990
Willson, R. F., & Folch-Pi, F. J. 1981, AJ, 86, 1084
Wolf, G. A., Lada, C. J., & Bally, J. 1990, AJ, 100, 1892
Wood, D. O. S., & Churchwell, E. 1989, ApJS, 69, 831
Wright, E. L. 1976, ApJ, 210, 250
Zinnecker, H., Bastien, P., Arcoragi, J., & Yorke, H. W. 1992, A&A, 265, 726